Void Detection Demonstrations
at the
Colorado School of Mines
Edgar Experimental Mine

Prepared for
U.S. Department of Labor
Mine Safety and Health Administration
1100 Wilson Boulevard, Suite 2132
Arlington, VA 22209

by the
Western Mining Resource Center
Colorado School of Mines
Golden, Colorado 80401

January, 2007

Void Detection Demonstrations at the Colorado School of Mines Edgar Experimental Mine

TABLE OF CONTENTS

1.0 INTRODUCTION

Significant hazards to miners are created when active workings approach mined-out areas of either the same mine, or mines located adjacent, above, or below the active mine. Potential hazards include water or toxic gas inundation of the active workings. These previously mined-out areas may be unintentionally penetrated if information pertaining to their location is not accurate or available to mine operators.

Although there are current regulations at the state and federal level addressing the accurate surveying and mapping of mine workings as well as the long-term archival of mine maps, this was not the case prior to approximately 1970. Many of the abandoned mines were in operation prior to the regulations and have not been accurately surveyed, mapped, or documented. In addition, many of the maps that have been created cannot be located.

Mine Safety and Health Administration (MSHA) records show that since 1995, there have been over 100 reported incidents where active mines have inadvertently cut into mined-out areas. Unavailable, inaccurate, or incomplete mapping of older abandoned mines is typically responsible. Many additional incidents have not been officially reported because no injuries or other significant consequences resulted. These incidents continue to occur as mine operators attempt to recover coal reserves that may be located near abandoned mines.

A mine operator is presently required to identify any adjacent mine that will be within 1,000 feet of the projected workings of the proposed mine. However, investigation of recent inundation incidents has found that maps of abandoned mines have been off by as much as 3,000 feet, meaning that maps alone cannot reliably ensure that inundation will not occur.

Geophysical techniques offer means to detect the presence of old mine workings at a resolution that may be far superior to old mine maps. In this report, the results of void imaging using cross hole seismic tomography, borehole ground penetrating radar (GPR), and cross hole GPR tomography methods are presented. These geophysical surveys were conducted at the Colorado School of Mines (CSM) Edgar Mine experimental facility, located in Idaho Springs, Colorado. The purpose of these investigations was to map the location of a known mine void.

2.0 SCOPE OF WORK

The scope of work undertaken for this project is in accordance with MSHA contract award No. B2532537, dated October 8, 2004. Specific tasks performed include:

- Construction of a reinforced shotcrete bulkhead to permit void detection demonstrations to be performed under air, then water-filled conditions;
- Deviation measurements of two boreholes utilized for the geophysical imaging;
- Cross hole seismic tomography investigations under air and water filled void conditions;
- Borehole GPR surveys under air and water filled void conditions;
- Cross hole GPR tomography investigations under air and water filled void conditions;
- Data processing and interpretation; and
- Preparation of this summary report.

Blackhawk, a division of Zapata Engineering was subcontracted by CSM to conduct the cross hole seismic tomography investigation. Additionally, Geo-Recovery Systems, Inc. was subcontracted by CSM to assist in carrying out the GPR investigations. Initial field investigations were carried out from September to October of 2005, and supplementary cross hole seismic tomography investigations were conducted in January of 2006.

3.0 EXISTING SITE CONDITIONS

The Colorado School of Mines (CSM) experimental mine, known as the Edgar Mine, was one of the very rich gold and silver mines in the Idaho Springs mining district. The Edgar Mine was named after the Edgar mineral vein that traverses the hillside above the mine. CSM acquired the mine in 1921, when officers of the then bankrupt Big Five Mining Company, agreed to lease the mine to the school. CSM has since acquired additional land and workings to form the present holdings of the Edgar Mine, which are now the property of the school. As shown in Figure 1, the Edgar Mine is located approximately 30 miles west of Denver in the town of Idaho Springs

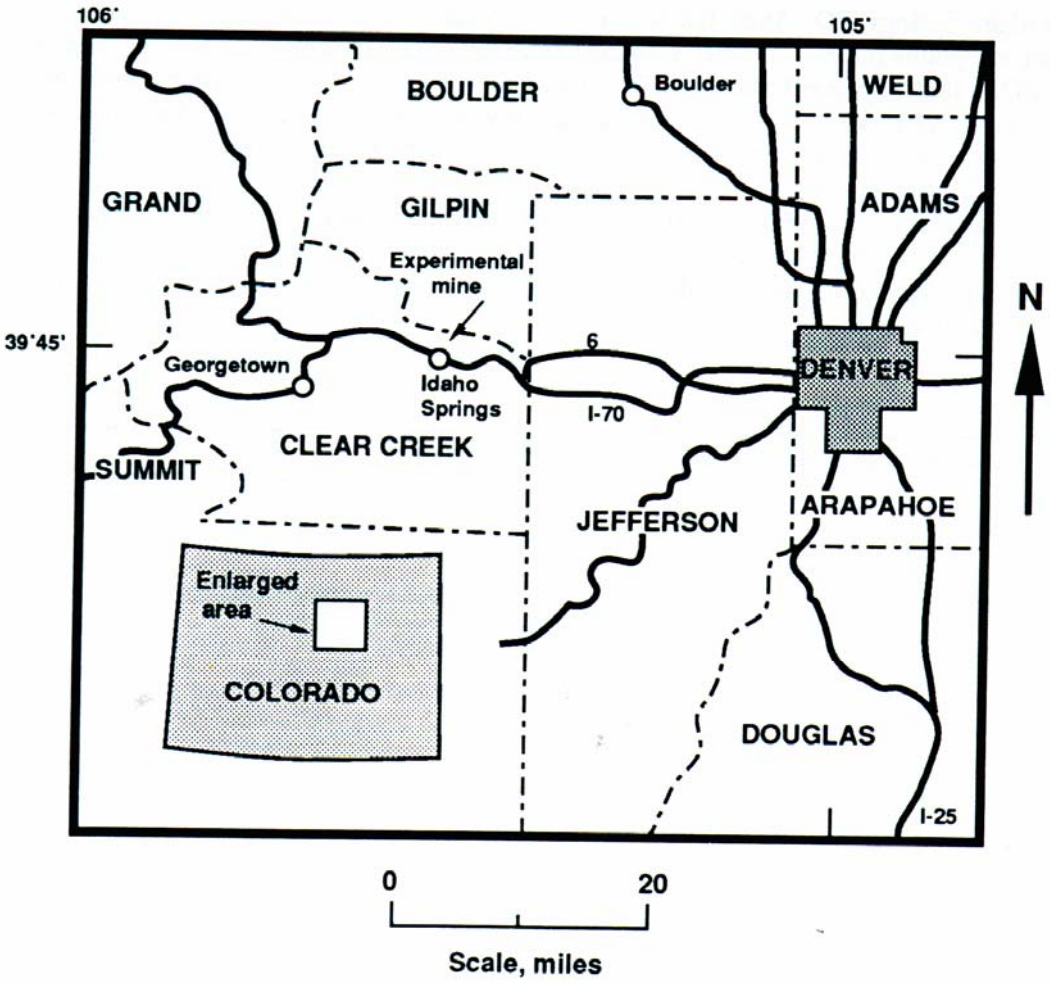

Figure 1. Edgar Mine location map.

As shown in Figure 2, the mine workings are accessed via separate portals to the Miami Tunnel and Army Tunnel. Driving of the Miami Tunnel commenced in the 1890's to access the Edgar's silver vein. The Army Tunnel and Army North Drift were driven less then 20 years ago to perform the U.S. Army's Korean tunnel detection experiments.

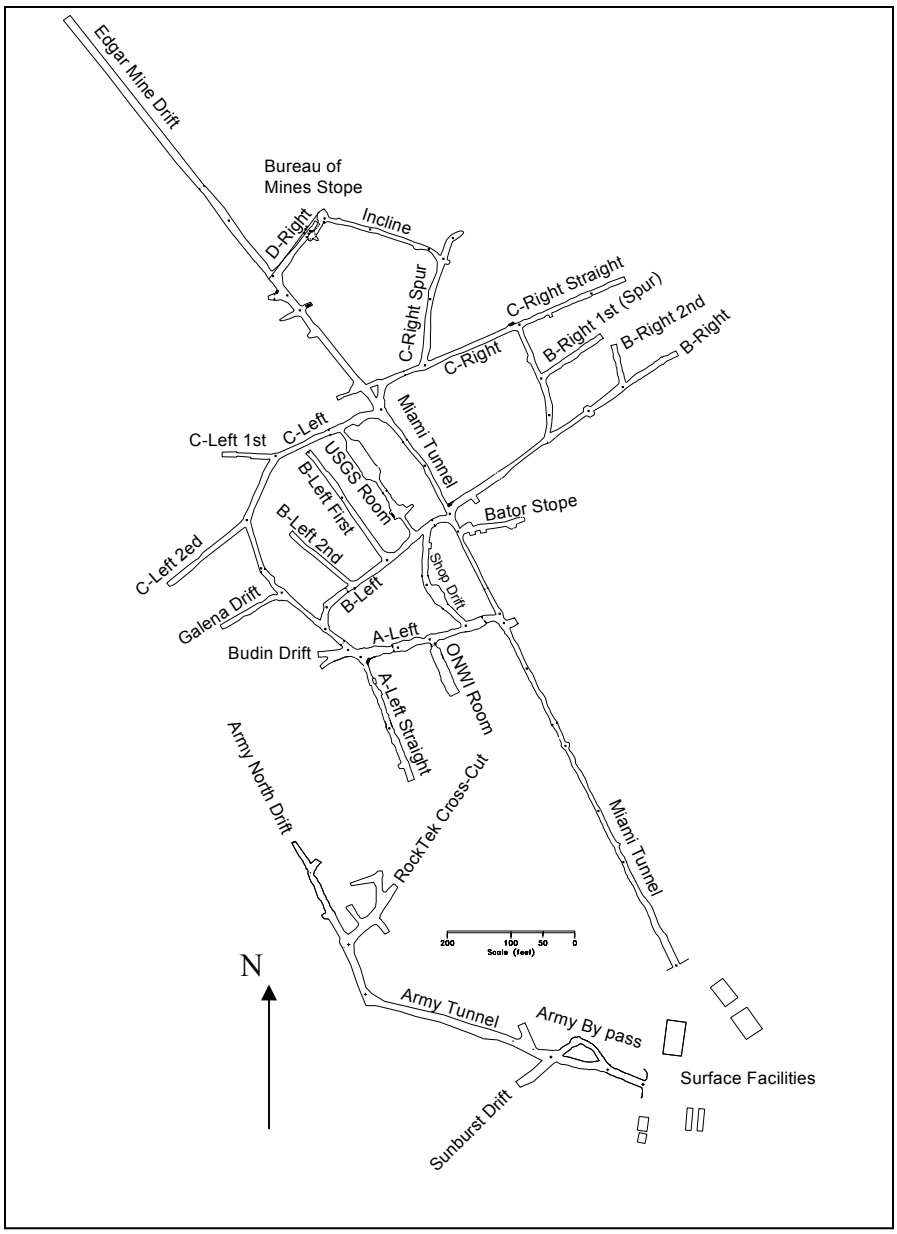

Figure 2. Layout of Edgar Mine workings.

The underground workings of the Edgar Mine comprise a network of horizontal openings having a cumulative length of approximately 1.4 miles. Lengths of individual openings

vary from less than 30 feet to approximately 1900 feet, and the cross-sectional dimensions range from about 8-feet wide by 8-feet high, to 15-feet wide by 15-feet high.

During the past 80 years, the Edgar Mine has been used by private companies and various state and federal agencies to develop a wide range of products and concepts. Some of the more notable research projects that have been preformed at the mine include:

- The U.S. Army's Korean tunnel detection program;
- The National Institute for Occupational Safety and Health's rock burst detection method development program;
- The rock mechanics data acquisition methods study for the Department of Energy;
- An in-situ stope leaching project performed by the former U.S. Bureau of Mines;
- Ventilation research for MSHA.

On the surface above the mine site, there are existing boreholes that were used for the Korean tunnel detection research. The boreholes range from four to ten inches in diameter and extend to depths up to approximately 500 feet. Most of the boreholes are adjacent to the trace of the Army Tunnel and Army North Drift (Figure 2), where the void detection demonstrations for this project were undertaken.

3.1 Geologic Overview

The Edgar mine extends through Precambrian rock units which have been subjected to three or more episodes of structural deformation. As shown in Figure 3, principal rock types include quartz-plagioclase gneiss, quartz-plagioclase-biotite gneiss, quartz-biotite-hornblende gneiss and biotite-microcline pegmatites. The mine is situated on the steeply dipping northwest flank of a northeastward trending anticline and contains many small fault zones. The fault zones generally strike in a northeast direction and dip to the north between 30 and 80 degrees. The rock mass in the area of the mine has at least three joint sets, and in localized areas up to five joint sets. Rocks encountered in the Edgar Mine are generally very competent, being characterized by the geomechanical properties summarized in Table 1.

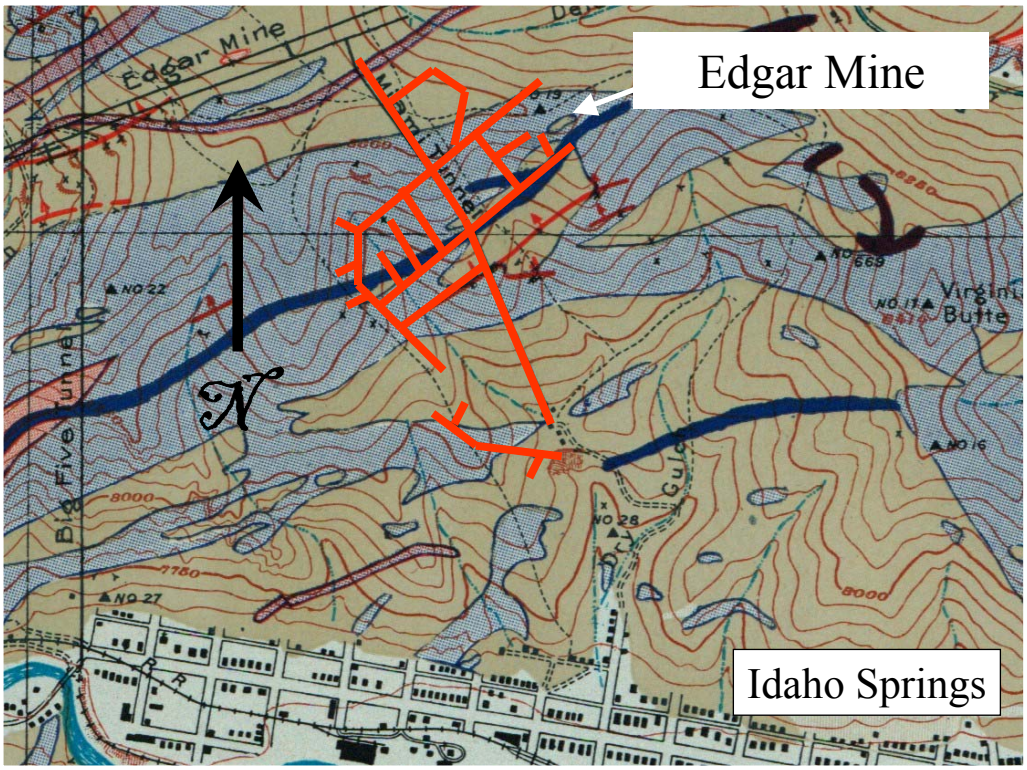

Explanation:

Light Blue: Precambrian quartz-plagioclase gneiss and quartz-plagioclase-biotite gneiss

Brown: Precambrian quartz-biotite-hornblende gneiss and biotite-microcline pegmatites.

Black and Purple: Tertiary porphyry dikes

Dark Blue: Silver veins

Red: Approximate location of the Edgar Mine Workings

Figure 3: Edgar Mine geology map.

Table 1. Typical geomechanical properties of rocks encountered in the Edgar Mine.

Uniaxial Compressive Strength	40 – 150 MPa
Elastic Modulus	60 to 90 GPa
Poisson's Ratio	0.2
Joint Friction Angle	30^{o} to 45^{o}
Rock Mass Rating (RMR)	40 to 80

4.0 MINE IMPROVEMENTS

In order to permit void detection demonstrations to be performed under air and water filled void conditions, a reinforced shotcrete bulkhead for this project was designed by Lachel, Felice & Associates and constructed by Mining & Environmental Services LLC. As shown in Figure 4, the bulkhead is located within the Army Tunnel, where it isolates an approximately 100 foot length of drift. All void detection demonstrations were performed using existing boreholes U1A and U5, which have surface coordinates and depths as summarized in Table 2.

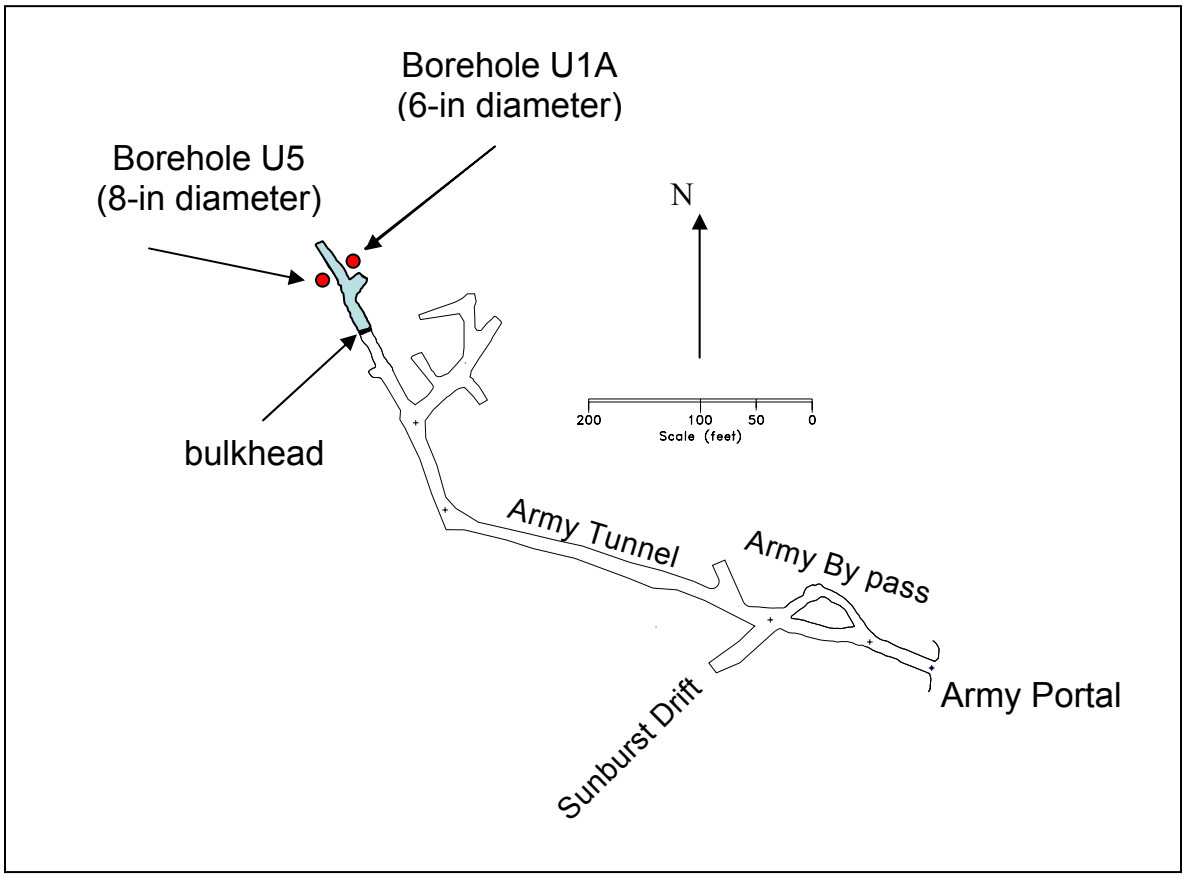

Figure 4. Location of bulkhead and the boreholes utilized for void detection demonstrations.

Table 2. Surface coordinates and depths of Boreholes U1A and U5 (Coordinates in Colorado Central State Plane)

Borehole	Northing (ft)	Easting (ft)	Elevation (ft)	Depth (ft)
U1A	3124.08	6938.58	8079.29	275
U5	3113.16	6904.85	8084.66	314

As shown in Figure 5, the drift within the area isolated by the bulkhead (and along a section between Boreholes U1A and U5) has an approximately square cross section, with average edge dimensions of approximately 11 feet. Photographs of the bulkhead during construction operations are shown in Figures 6a and 6b. Rock surfaces within the isolated section of the tunnel were left bare, and when filled, the water surface elevation corresponded to the vent pipe inverts shown in Figures 6a and 6b.

Figure 5. Army Tunnel conditions prior to bulkhead construction (future bulkhead location indicated by sidewall anchor bolts).

Figure 6a and 6b. Bulkhead conditions during construction (note vent pipes at top of bulkhead).

5.0 VOID DETECTION DEMONSTRATIONS

5.1 Borehole Deviation Surveys

To provide necessary spatial constraint for the void detection demonstrations, deviation surveys were performed for Boreholes U1A and U5 by the Colog division of the Lane Christensen Company. The results of the deviation surveys are shown in Figures 7 and 8, and these results were utilized for proper processing of all cross hole and borehole geophysical surveys. Referenced from the top of the boreholes, U1A deviated approximately 3.17 ft to the south and 0.97 ft to the east, and borehole U5 deviated approximately 4.67 ft to the west and 0.59 ft to the north.

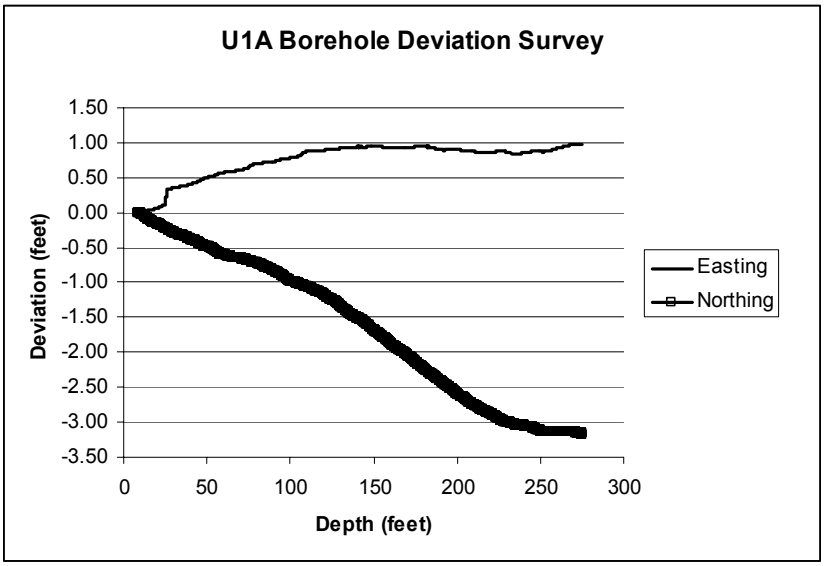

Figure 7. Borehole deviation survey results for U1A.

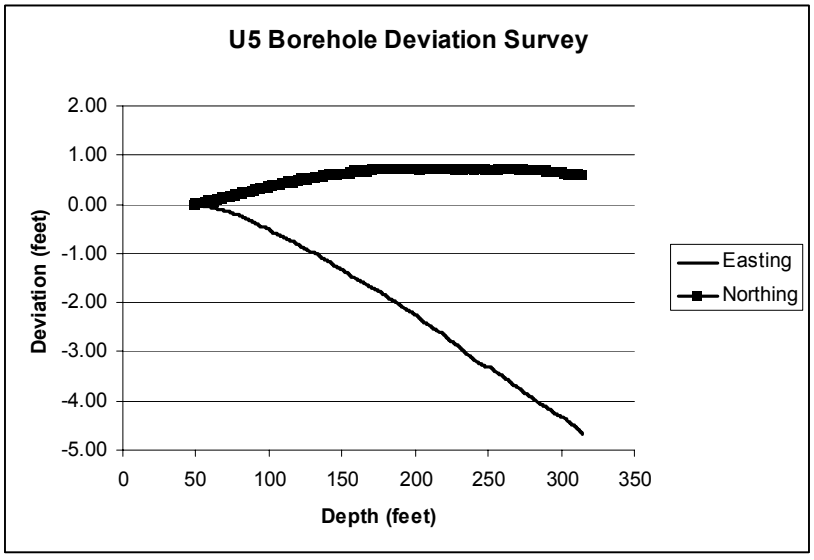

Figure 8. Borehole deviation survey results for U5.

5.2 Cross hole Seismic Tomography

The objective of this investigation was to conduct two-dimensional cross hole seismic tomography surveys in order to map the location of the tunnel void between Boreholes U1A and U5, and to assess any variation in the dataset corresponding to air and water filled void conditions.

5.2.1 Basic Concept and Theory

Cross hole seismic tomography (XHST) is used for high-resolution imaging of the subsurface between boreholes. Tomography is an inversion procedure that provides for 2-D and 3-D velocity and/or attenuation imaging between boreholes from observation of transmitted first-arrival seismic energy.

Tomography data collection, as shown in Figure 9, involves scanning the region of interest with many combinations of source and receiver depth locations, similar to a medical Computerized Axial Tomography Scan (CATscan). Typical field operation consists of placing a string of receivers (geophones or hydrophones) at the bottom of one borehole and moving the source systematically in the opposite borehole from bottom to top. The receiver string is then moved to the next depth interval and the test procedure is repeated until data from all possible source-receiver combinations are obtained.

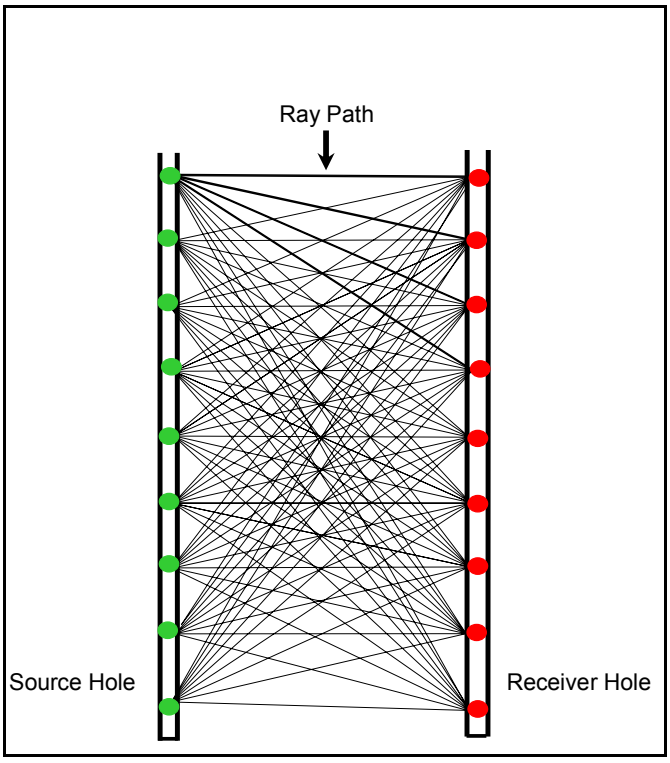

Figure 9. Basic principle of the HXST technique.

The use of tomographic analysis for imaging geological boundaries between boreholes has become a well-established technique in geophysical investigations. It involves imaging the seismic properties from the observation of the transmitted seismic wave (compressional P-wave or shear S-wave), first arrival energy in either time or amplitude. The relationship between the velocity field v (x, y) and travel time t_i is given by the line integral (for a ray i):

Equation #1 $$t_i = I_{Ri}\, ds / v\,(x,y)$$

Where R_i denotes the curve connecting a source-receiver pair, which yields the least possible travel time according to Fermat's principle. Tomography is an attempt to match calculated travel times (model responses) to the observed data by inversion of these line integrals. Initially, the region of interest is divided into a rectangular grid of constant velocity cells (j) and a discrete approximation of the line integral is assumed as:

Equation #2 $$t_i = 3_j\, \Delta S_{ij} \,.\, n_j$$

Where ΔS_{ij} is the distance traveled by ray i in cell j, and n_j slowness within cell j. Using a first order Taylor expansion and neglecting residual error, Equation #2 can be written in matrix form as:

Equation #3 $$\underline{y} = A\,\underline{x}$$

Where the vector $\underline{y}$ is defined as the difference between computed travel times (from the model) and the observed travel times, vector $\underline{x}$ is the difference between the true and the modeled slowness, and A is the Jacobian matrix. In travel time tomography, Equation #3 is solved using matrix inversion techniques.

The seismic wave field is initially propagated through a presumed theoretical model and a set of travel times is obtained by ray-tracing (forward modeling). The travel time equations are then inverted iteratively in order to reduce the root mean square (RMS) error between the observed and computed travel times. The inversion results can be used for imaging the velocity (travel time tomography) and attenuation (amplitude tomography) distribution between boreholes.

Two types of tomographic processing are generally used, including:

- Travel Time/Attenuation Tomography – Uses time of flight (first-arrival travel times and amplitudes) to derive velocity/attenuation images using inversion techniques.

- Reflection Tomography – Uses the reflection/diffraction events in the data for the seismic imaging of target zones using migration or vertical seismic profile (VSP) techniques.

Table 3 lists underlying factors that are necessary to consider when performing XHST surveys.

Table 3. XHST criteria

Criteria	
Maximum Imaging Depth	Penetration depth is up to 1,000 ft in hard rock between three to four inches I.D. PVC-cased and grouted boreholes, or open holes in bedrock. Sources range from borehole hammer and vibrators for short offsets, to sparkers and air guns for larger offsets.
Contents of Detected Voids	Voids are suitable targets for tomography; however, the tomography technique is generally unable to determine the content of voids. For water-filled voids, poor tomographic images of the void may be obtained if a low velocity contrast exists between the water and the surrounding geologic materials.
Performance Handling Characteristics (Effective frequency range, wave attenuation, and	The measured frequency content of the cross hole signal depends upon the type of soil and rock at a site, and on the seismic source. In general, frequencies recovered are on the order of 40-600 Hz. Resolving power and resolution are a function of wavelength, which is in turn a function of the propagation velocity and frequency of the seismic signal. Typically, wavelengths are on the order of two to 20 feet.

the size and orientation of void)	Generally, the frequency of the seismic signal decreases as the borehole separation increases. For small target zones, the offset between the source and receiver boreholes must be short enough to provide a sufficient travel time delay to resolve the anomaly created by the target. Also, modeling prior to survey design is beneficial to compute the expected magnitude of the travel time anomaly, which will aid in the design of the data acquisition parameters required to adequately image the target. Borehole design is also a factor. For proper imaging, the source-receiver borehole pairs must be placed around the suspected target zone and be drilled to depths equal to at least 1.5 times the source-receiver spacing below the expected depth of the target. In other words, if the separation between source-receiver holes is 35 ft and the target depth is 200 ft, then the boreholes should be drilled to minimum depths of 253 feet. If large horizontal offsets are used between the source and receiver boreholes, low vertical resolution will be obtained in the tomograms, resulting in the velocity images being elongated in the horizontal direction.
Repeatability of Test Results	Tomographic results are generally very repeatable if the integrity of the borehole walls is maintained.
Data Integrity and Interpretation	**Ease and Reliability of Data Gathering-** A geophysicist should design the survey and oversee data acquisition for quality control**.**
	Data Processing - Processing is done by geophysicists that specialize in cross hole seismic tomography processing. Well logs, known depths, results from ancillary methods, and the expected results should be furnished to the processor to aid in data processing and interpretation.
	Data Interpretation - Voids are identified in velocity tomograms as low velocity zones in most geologic settings. However, proper volumetric imaging of voids must be done by a qualified geophysicist to identify possible image distortions due to velocity anisotropy and presence of artifacts near image boundaries.

5.2.2 Limitations of XHST

Table 4 lists the limitations of the XHST in various geologic, geographic and environmental conditions, including data acquisition and processing.

Table 4. Limitations of the XHST

Geologic, Geographic, and Environmental Condition Limitations	
Diverse Environmental Compatibility	In general, environmental limitations are related to the drilling operations and not the XHST data acquisition or its systems.
Groundwater Conditions and Saturated Zones	If the void is water-filled and the geologic materials are poorly lithified, the velocity contrast between these two media will be diminished and the void could be undetectable with P-wave XHST.
Subsurface Features	Vertical planar features (e.g., high-angle faults, fractures, etc.) between vertical borings are difficult targets to image uniquely. In addition, tomographic imaging is unreliable at the top and bottom of the tomogram because of limited ray path coverage, and the inversion algorithms typically place artifacts in these areas of poor coverage.
Void Contents (i.e., Water, Air/Gas, Slurry or Gob)	Void contents affect the velocity contrast between the void and the surrounding geologic materials. This directly affects the ability of XHST to image and resolve the voids.
Acquisition and Processing Limitations	
Data Analysis and Interpretation	Processing of the XHST data requires the use of specialized software, and personnel experienced in the analysis of the seismic data. An understanding of the geology of the site is also required to ensure that the tomogram produced is consistent with the geologic conditions at the site. While the presence of the void can be determined by looking for anomalous low velocity zones within the tomogram, determining the extent of the void requires an analysis of the frequency content and the velocities of the surrounding strata.
Disruption of Normal Mining Operations	XHST data acquisition creates a disruption to the mine if mining activities are on-going in the immediate vicinity of the drilling. Coordination is required to schedule the drilling around the mining activities.
Site Preparation	Boreholes must be drilled with care to minimize drift with depth and to minimize borehole wall damage. Deviation surveys must be conducted to map deviation of each borehole. Borehole completion is a critical step; with poor borehole completion (i.e., improper placement of casing and grout), the seismic data

	can be rendered useless. ASTM has a standard (D4428/D4428M-00) for completion procedures to be used for cross hole seismic tests. If these procedures are adhered to, the data should provide useful subsurface velocity information. Borehole layout also is a factor. Borehole separation-to-depth ratio should be about 1:2 for seismic tomography imaging.

5.2.3 Data Acquisition

The XHST survey was performed to image the Edgar Mine's Army Tunnel along a section line between Boreholes U1A and U5. The Army Tunnel Portal at the Edgar Mine is shown in Figure 10, and the Army Tunnel Layout, together with the locations of Boreholes U1A and U5, are shown in Figure 4.

Figure 10. Army Tunnel Portal at CSM's Edgar Experimental Mine.

The XHST data were acquired in two separate phases (Phase I & II). Within each phase there were two separate surveys: 1) the first survey was conducted with an air-filled void condition, and 2) the second survey was conducted with a water-filled void condition. There was a delay between each of the surveys in order for water to be pumped behind the shotcrete bulkhead to fill the void. The duration of the field work for each separate survey was approximately one day. The XHST surveys were performed during the time periods summarized in Table 5.

TABLE 5. SCHEDULE OF XHST FIELD ACTIVITY

Field Date	Tasks Performed
Phase I	
September 22-23, 2005	Cross hole tomography survey for air-filled condition.
October 1, 2005	Cross hole tomography survey for water-filled condition.
Phase II	
January 3, 2006	Repeated cross hole tomography survey for air-filled condition
January 13, 2006	Repeated cross hole tomography survey for water-filled condition

As shown in Table 5, Phase I was conducted from September 22 through October 1, 2005 and used the Etrema vibratory source (Figure 11). After a review of the data and an initial attempt at processing the data, it was determined that recorded signals were dominated by electronic cross-feed of the signal sent to drive the source, and the data were not of sufficient quality to process as a XHST data set.

Phase II, a repeated survey, was conducted from January 3 through January 13, 2006 and used a sparker source (Figure 12). The data quality for this survey was much higher quality and the first arrival times of the data could be interpreted reliably. Therefore, this data set was suitable for processing as an XHST data set.

Figure 11. Etrema swept frequency seismic source.

Figure 12. Sparker seismic source.

The cross hole tomography survey was conducted between the two existing boreholes U1A and U5, having surface coordinates as summarized in Table 2. The offset between the source and receiver boreholes is approximately 35 ft at the ground surface. It is noted that this 35 ft borehole offset made use of existing boreholes, and void imaging at other borehole distances was beyond the scope of work authorized for this project. Logs of these boreholes were not available for our evaluation. The top of the target void for the survey is located at an elevation of 7879 ft, or at an approximate depth of 200 ft below ground surface. The average dimension of the void is approximately 11-ft by 11-ft in the 2-D plane formed by connecting the survey boreholes. It should be noted that the void geometry, as shown in Figures 5 and 6, has irregular shape and its size can very by several feet. This site was well suited for the evaluation of the XHST method because the depth and dimension of the void is well known. Survey data was collected with the equipment and acquisition parameters summarized in Table 6.

Table 6. XHST data acquisition and equipment parameters

Acquisition System	Geometrics Stratavisor NX 60 channel - 0.25 ms sampling and 64 ms record length
Seismic Source	1st Attempt: Etrema Swept Frequency Source with Agilent Signal Generator and 250 watt amplifier sweeping 40 to 500 Hz.
	2nd Attempt: Down hole Sparker using Applied Acoustics CSP1500 Signal Generator – 3 source stacks per station at 800 joules output per shot
Source Interval	3 feet
Hydrophones	Oyo Geospace 12 channel @ 3-ft spacing and/or Benthos 24 channel string @ 1-m spacing

As discussed above, an initial attempt was made to acquire the dataset using the Etrema swept frequency source. However, the data quality was insufficient to accurately pick the travel time (first breaks.) We believe that the reasons for this were as follows:

1) There was a significant amount of crosstalk from the Etrema source amplifier that appears to be significantly higher in amplitude than any seismic signal received by the hydrophones. This problem was not detected during data acquisition because correlation was not possible in the field,
2) Due to the close spacing of the boreholes and the high seismic velocities of the rock strata surrounding the void, the first arrival time is very close to the beginning of the records (less than 5 ms), when using a vibratory source such as the Etrema, the correlated wavelet can be truncated by the beginning of the record.

Our first choice was to use a sparker or air gun seismic source because the use of a swept frequency source can lead to the problems described above; however, none of the sources were available to us during the time frame of the original field effort, resulting in using the Etrema vibratory source.

The data were obtained by lowering the hydrophone string in borehole U5 and then acquiring seismic records with the source located at different depths in borehole U1A.

To facilitate source and receiver performance, water was added to the initially dry boreholes. As shown schematically in Figure 13, data were acquired over depths in the boreholes corresponding to about 51 feet above to 63 feet below the target void (approximate survey elevations 7930 to 7805 feet).

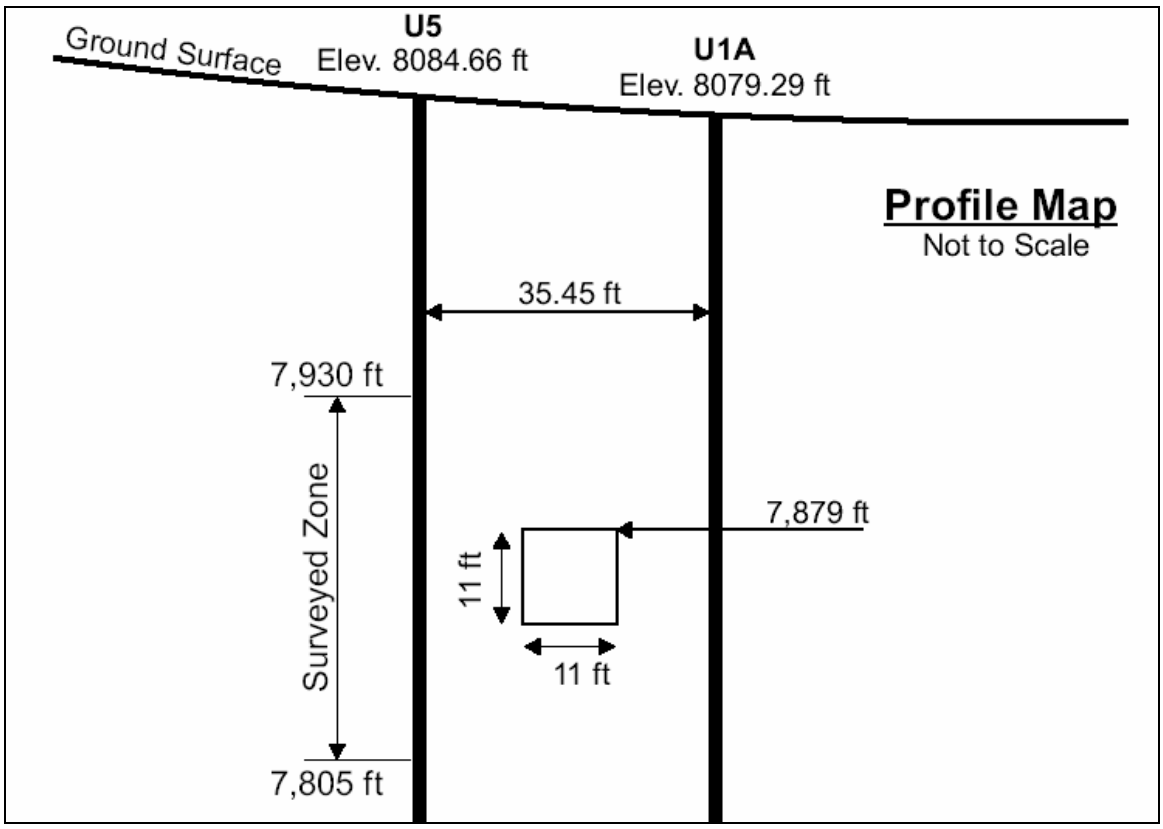

Figure 13. Schematic vertical profile of boreholes U1A and U5, the target void, and surveyed zone.

Figure 14 shows the 24-channel hydrophone array being lowered in borehole U5, and Figure 15 shows the data acquisition setup and water being added to borehole U1A.

Figure 14. The 24-channel hydrophone array.

Figure 15. Data acquisition setup, with water being added to borehole U1A.

5.2.4 Data Processing and Interpretation

The survey data, corrected for borehole deviations, were imported into Oyo Seisimager, where the source and receiver geometry were applied and the first arrival times picked. The first arrival time files were then exported, reformatted and input into GeotomCG,

where the final tomograms were generated. The data were also processed using a second tomography software package by Summit Peak Technologies (SPT). The tomograms from SPT provided no additional information compared with the GeotomCG results and therefore were not included in this report. GeotomCG uses the simultaneous iterative reconstruction technique (SIRT) algorithm (Lytle et al., 1978; Peterson, et al., 1985). The SPT uses a proprietary full-wave form tomography algorithm.

GeoTomCG allows for 3-D processing and can account for positional variation based on borehole deviation data. The basic data processing flow included the following:

- Import data;
- Frequency filter to remove noise;
- Pick first breaks;
- Apply geometry and import into tomographic software package;
- Edit data for outliers;
- Create starting model (average constant velocity);
- Set inversion parameters (curving ray, velocity limits, number of iterations);
- Invert data while observing changes in RMS error and residuals;
- Determine appropriate number of iterations;
- Export final model;
- Edit final model format and import into Geosoft Oasis;
- Grid and display model; and
- Export final image.

The final inversion parameters that appeared to give the best results were:

- 5 Straight ray inversion steps, followed by up to 10 curved ray;
- Velocity constraints of no less than 5,000 ft/sec and no more than 18,000 ft/sec;
- Pixel size of 1 m was used based on the spacing of the shots and receivers;
- Final RMS (root mean square) residuals for the GeotomCG inversions were on the order of 3.5E-04.

The sparker source provided good signal amplitude and high frequency response. Figure 16 shows an example shot record recorded during the field survey. The source was positioned at a depth of 197 ft and the hydrophone receivers were positioned between 182 ft and 215 ft depth. The trace spectra of this shot record are shown in Figure 17. The spectra show that the sparker produced recorded signals with frequencies ranging from about 400 Hz to 1,500 Hz. The dominant frequency of the first arrival of energy in the shot record is approximately 1,000 Hz.

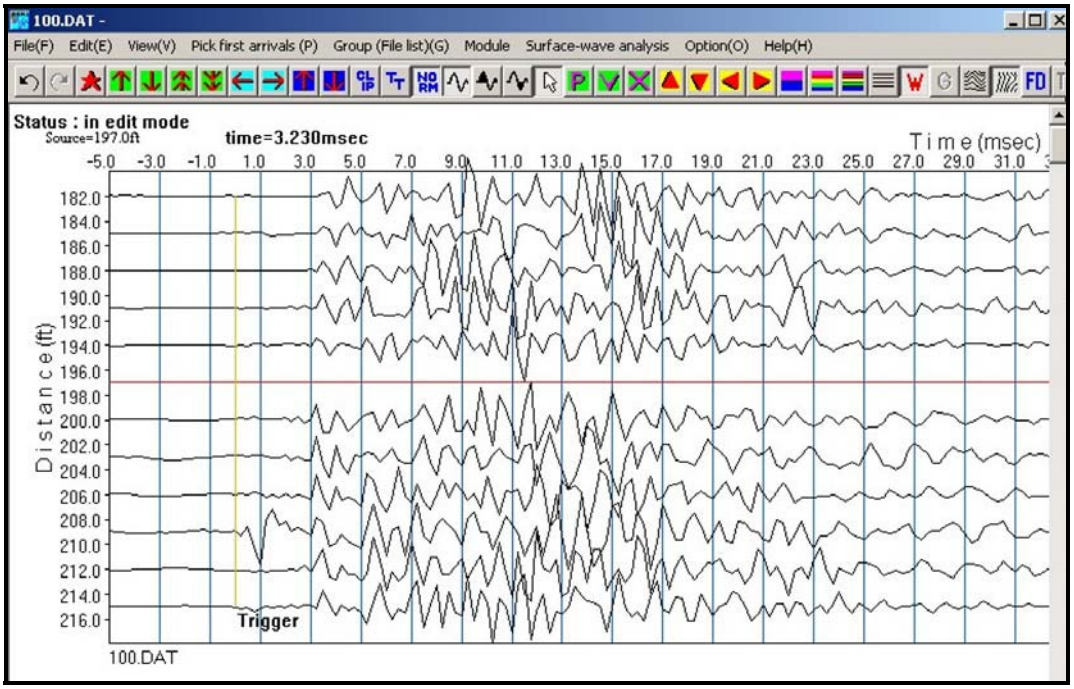

Figure 16: Sample shot records using the sparker source and hydrophone string.

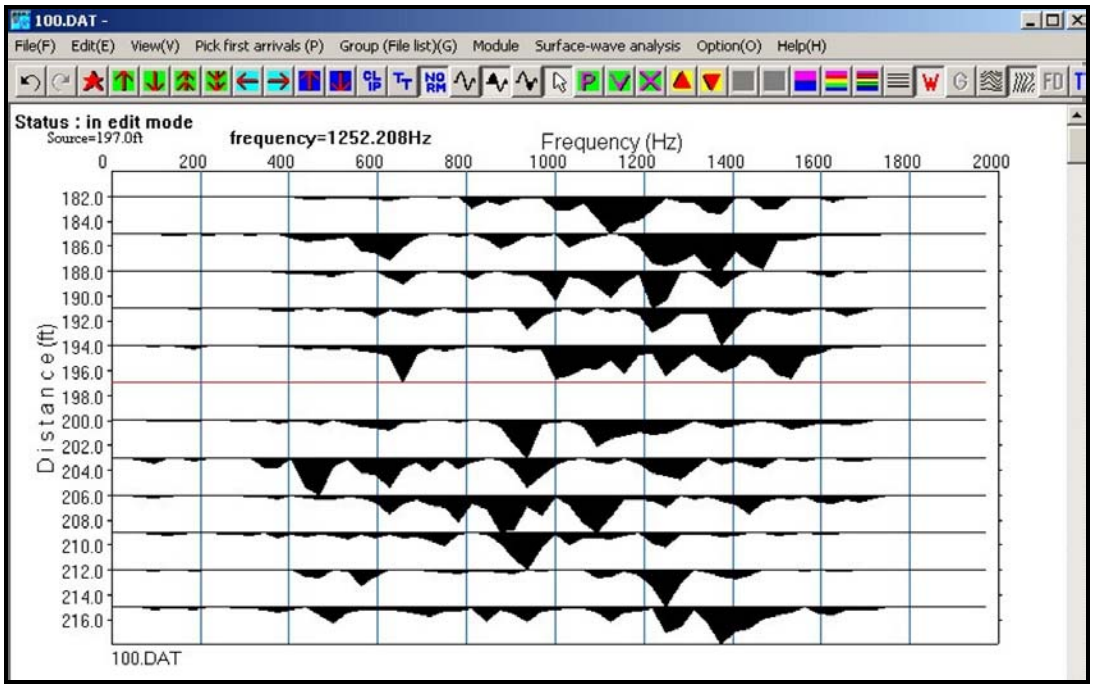

Figure 17: Individual trace spectra derived using Discrete Fourier Transform.

Source time repeatability was visually monitored during data acquisition, but specific repeatability test records were not recorded. During the survey, three shots were stacked (vertically summed) for each shot record. Good repeatability of source timing can be

inferred by the high frequency signals found in the spectra of the shot records. Stacking shots using a source with poor repeatability in shot timing produces summed records with coherent signals (i.e. first arrivals) that have lower effective frequency content than found in a single shot record. The high frequency of the stacked data suggests good source timing repeatability.

Figure 18 and 19 show the 2-D velocity tomograms between boreholes U1A and U5 for the air- and water-filled void conditions, respectively. Lower velocity zones in the tomograms are shown as "cooler" colors (blue and green), and higher velocity zones in the tomograms are shown as "warmer" colors (red and pink). The low velocity anomaly interpreted as the void in Figure 18 for the air-filled void is approximately located in the center of the tomogram with the top of the anomaly at an elevation of about 7887 feet. The low velocity anomaly interpreted as the void in Figure 19 for the water-filled void is approximately located in the center of the tomogram with the top of the anomaly at an elevation of approximately 7882 feet. As a comparison, the true top of void elevation is at an approximate elevation of 7879.

The accuracy of the void location was better with the water-filled void than the air-filled void condition. This is likely due to less attenuation of the signal prorogating through the rock strata surrounding the water-filled void than the air-filled void condition. Therefore, the travel time measurements were more accurate, allowing a better inversion. The presence of water in the rock fractures surrounding the void, due to water seepage, may have improved signal to noise because of decreased attenuation. This would result in better tomographic inversions.

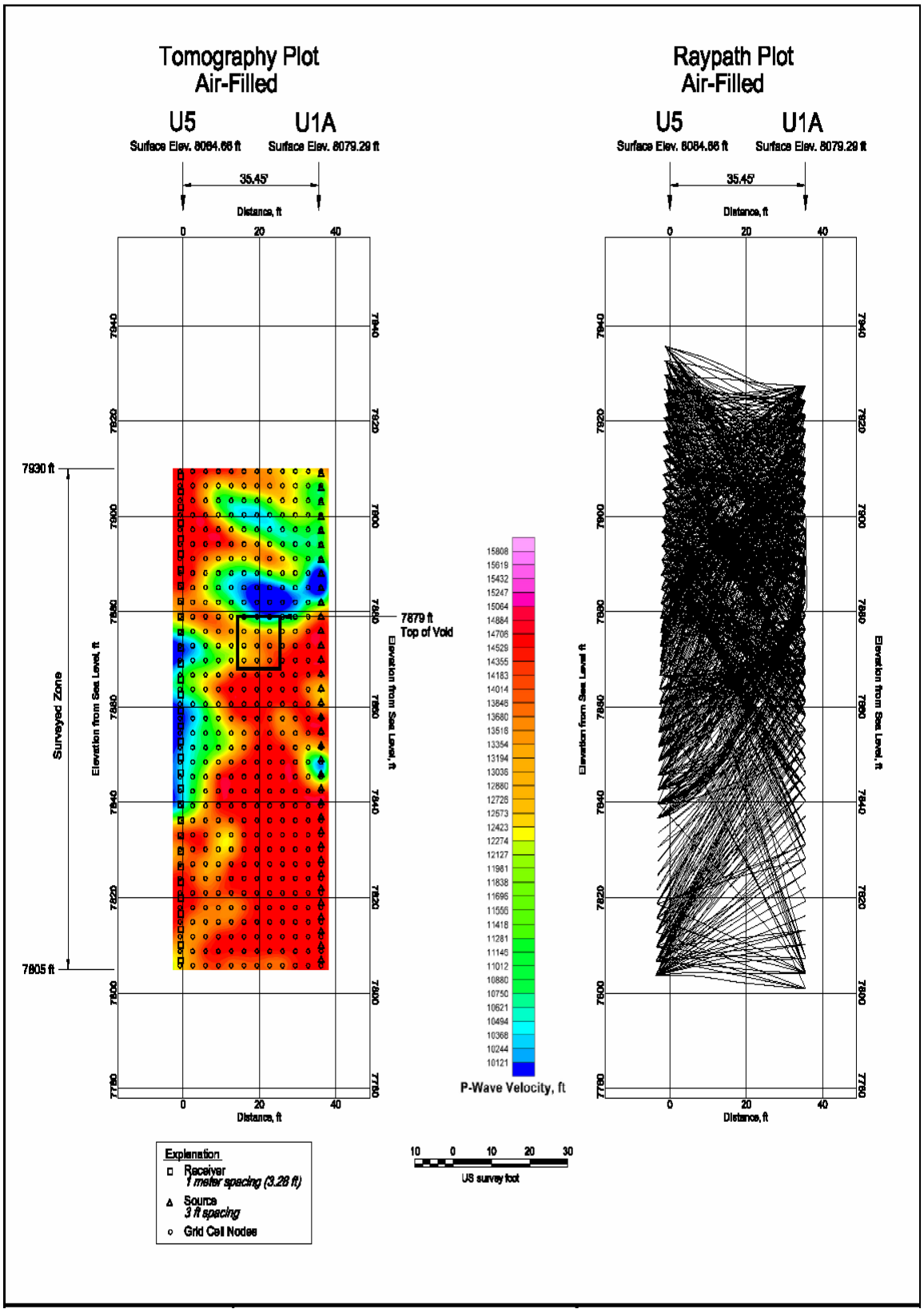

Figure 18. Two-dimensional tomogram image for the air filled void condition.

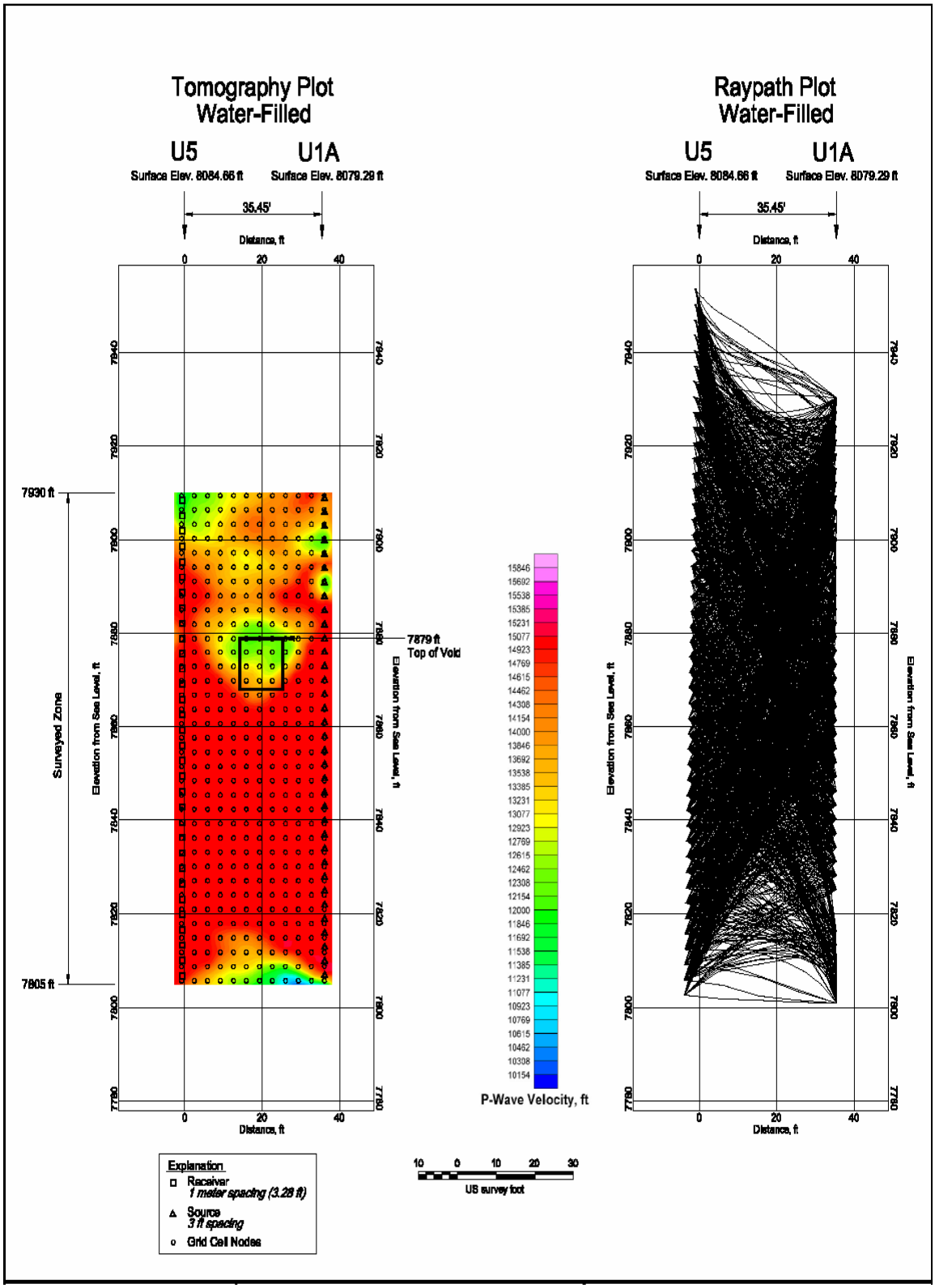

Figure 19. Two-dimensional tomogram image for the water filled void condition.

5.3 Borehole Radar Survey

The objective of this investigation was to conduct a borehole radar survey in order to map the location of the tunnel void from Borehole U1A, and to assess any variation in the dataset corresponding to air and water filled void conditions.

5.3.1 Basic Concept and Theory

The ground penetrating radar (GPR) method uses the propagation of electromagnetic energy at radio frequencies (1 to 3,000 MHz) to determine characteristics of the earth materials through which the energy passes. The GPR system measures received amplitude as a function of travel time from the time zero when the transmitter fires. From these data, information on the electromagnetic velocity, attenuation, and dispersion of the materials may be determined.

In the borehole GPR method, the transmitter and receiver are positioned in the same borehole and the system operates in the reflection mode. The interpretation of the radar returns allows the distance to a reflector (e.g. void) to be determined if the geological material between the borehole and the void has a known or measurable velocity. If the reflector is planar, such as is the case for a rock fracture, the angle of the reflector can be determined. However, the direction of the reflector cannot be obtained since the borehole radar is omni-directional. To determine the direction of a reflector, data from more than one borehole is therefore required or a directional radar antenna must be used.

The Borehole GPR method transmits pulses of radio energy into the subsurface and receives the returning pulses that have been scattered (reflected, refracted or diffracted) from interfaces between materials with different electromagnetic properties. Antennas are moved through the borehole with a continuous series of radio pulses, producing a distorted cross-section of the subsurface. The distortion is a function of the geometry of the antenna position and orientation, as well as the velocity of the material properties in the subsurface. Correcting for antenna position and orientation by modeling removes the distortion to generate a true geometric cross section image of the variations of electromagnetic properties in the subsurface.

The key material properties are the dielectric permittivity, the magnetic permeability, and the electrical conductivity. The *dielectric permittivity* dominantly controls the velocity of electromagnetic wave propagation and is a function of the density, water content, and type of material. The *magnetic permeability* also controls velocity (the velocity is the reciprocal of the square root of the product of permittivity times permeability). Permeability is commonly neglected (assumed to be the value of air), though it may be important when iron-bearing materials are present. The pulse travels faster through a low

dielectric permittivity material (typically drier) than a material possessing a higher dielectric permittivity (more wet or dense).

The *electrical conductivity* is the main electrical parameter controlling the depth of investigation, and is the ability of the material to conduct electrical current which is dominantly controlled by the amount of water present and the concentration of ions in solution. The conductivity of the material dictates how quickly the pulse of radio energy decays in amplitude (attenuates) with distance and thus controls how deep the pulse will penetrate. In addition, the attenuation of the pulse with distance is attributable to spherical divergence as the energy density decreases as the waveform spreads out geometrically away from the antenna (like spreading the energy over the surface area of a balloon, being blown up and expanding in area with increasing size).

The dielectric permittivity and conductivity are mostly independent. For example, freshwater and salt water have essentially the same dielectric permittivity (salt water is slightly lower); however, salt water exhibits a much higher conductivity than freshwater. GPR pulses travel at similar speeds through both types of water; however, in salt water the energy is attenuated very quickly and does not penetrate deeply.

There are also additional losses possible from dielectric relaxation processes (such as the interfacial or orientation polarization of water), electrochemical reactions on the surfaces of clay minerals, surface and volume scattering, and magnetic relaxation processes. Penetration ranges from 5 kilometers in hard frozen polar ice to 30 meters in dry sand to less than 1 meter in a mineralogical clay like bentonite.

Reflections of the GPR pulse occur at boundaries in the subsurface where there are changes in the material properties. Only a portion of the pulsed signal is reflected and the remaining part of the pulse travels across the interface to again be reflected back to the receiver from another interface boundary. The time the pulse takes to travel through the layer and back is controlled by the thickness and electromagnetic properties of the material. The travel time between reflections can be used to calculate the distance to a reflector employing a known velocity.

5.3.2 Limitations of Borehole GPR

There are technical limitations to the use of Borehole GPR. The primary factor causing signal attenuation (and limiting depth of investigation) is the electrical conductivity of the material through which the radar energy passes. Materials with higher conductivity cause higher rates of attenuation. The Edgar Mine is situated in rock with relatively low

conductivity and the proposed distances of investigation posed no particular difficulties. However, where weathered, rock mass alteration has significantly increased losses from increased conductivity (higher water content, more conductive minerals) and heterogeneity (which increases scattering). Other limitations include inadequate knowledge of the location of the holes and of the radar tools in the holes, and resolution limitations for objects smaller than 1/3 of a wavelength or with inadequate tomographic angular coverage. (Wavelength is the velocity in the material divided by the frequency of the radar.)

5.3.3 Data Acquisition

A RAMAC/GPR system from Mala GeoSciences was employed for the Borehole GPR survey, using 100 MHz borehole antennas. These antennas have a wavelength of 3 m in air, 1.5 m in dry soil, 0.6 m in water saturated soil, 0.3 m in water, and about 1.2 m in the Edgar mine rock mass. The antenna housing and cable connection are waterproof, with 360 and 492 foot long control cables (the control cables are fiber optic, eliminating the need for wire cables which adversely affect the antenna performance). The electronics were powered by rechargeable batteries in the antenna housing. The operator console and up hole electronics for the RAMAC GPR system is shown in Figure 20, and the process of airwave transit time calibration is depicted in Figure 21.

Figure 20. The operator console (laptop computer) and up hole electronics (yellow box sitting on the shipping containers) for the Mala RAMAC borehole radar.

Figure 21. Holding the radar tool at top of hole for airwave transit time calibration.

The control cables worked in combination with a digital depth encoder to accurately determine down-hole transmitter and receiver positions. This digital distance information was utilized by the GPR control unit to maintain the distance between adjacent traces at even spacing intervals.

The GPR control unit was connected to the antennas via the control cables. The control unit was connected to a laptop computer, where Mala GeoSciences software provided selection of the survey and data collection parameters. The data were digitally recorded on a laptop computer in the field.

The borehole surveys were conducted before and after the target void in the mine tunnel was filled with water. Fractures connecting the boreholes and the tunnel caused water to also fill boreholes the near the tunnel depth. The surveys were accomplished by connecting the transmitter and receiver tools together and then acquiring data while lowering the antennas down a single borehole. These data were acquired via the RAMAC control unit and then stored on the laptop computer in the field. The radar data were examined in the field and unacceptable records were repeated until satisfactory results were achieved.

For the air-filled void conditions, the travel time range was set at 200 ns, and each trace was digitized to 512 16-bit samples. As the velocity of the radar wave is slower under

water-filled void conditions, the range was doubled to 400 ns, and each trace was composed of 1024 16-bit samples.

The data acquisition equipment was battery powered: the transmitting and receiving electronics used their internal battery-power, and the GPR system had an external battery supply. The data acquisition field laptop computer had self contained power, and a generator was used along with AC/DC adapters to keep the batteries power levels adequate for the survey demands.

To accomplish the surveys, the GPR was assembled such that the transmitter and receiver are connected to allow them to operate in a single borehole. The tools were connected to the control unit with a fiber optic control cable. The tool was placed in the borehole with the cable placed over a pulley supported by tripod. The pulley has a digital depth encoder so the position of the tool was known down the hole and allowed the data acquisition to keep the distance between adjacent traces at 0.5 feet.

Further details regarding Mala's radar data acquisition system, for both single borehole and cross hole surveys, are proprietary in nature, and thus cannot be published.

Completion of well logs from the surveyed boreholes, including gamma ray and electrical resistivity, was beyond the authorized scope of this investigation. Varying the water properties for the flooded void condition (e.g. with different amounts of soluble chemicals), and numerical feasibility studies to evaluate: (1) the reliability and interpretability of measurements; and (2) the distance limits at which radar surveys are able to detect the void, were also beyond the scope of authorized work.

5.3.4 Data Processing and Interpretation

The Borehole GPR data were processed to enhance the features in the GPR records using GRORADAR software. The processed data from borehole U1A is presented in Figure 22, which represents the total 275-foot length of the borehole. The left and right sides of Figure 22 correspond to the top and bottom of the borehole. These data are interpreted to show the target void at scan number 390, and with the distance the antennas traveled between traces at 0.5 feet, this places the center of the void at about 195 feet below the surface of Borehole U1A, corresponding to elevation 7884 feet. As a comparison, the true center of the void is located at approximate elevation 7874 feet.

The characteristic signature of a void usually appears as a diffraction pattern shaped like a hyperbola. In Figure 22, this hyperbola spans scan numbers 374 to 404 which corresponds to a vertical interval of 15 feet. The actual vertical void dimension is smaller

(11 feet), but the radar detects the void before it is inline with it because of the spreading wave front of the radar energy. The peak of the hyperbola occurs when the antenna is closest to the void, i.e., scan number 390.

To determine the distance between the borehole and the void, the two-way travel time can be converted to distance, using velocity. The two-way travel time corresponds to the time required for the radar pulse to travel to the reflector and back. From the data in Figure 22, the travel time is 50 ns. An estimate of the velocity for the conversion can be obtained from the dielectric permittivity. For the dry void tests the relative dielectric permittivity (permittivity relative to that of vacuum) was determined from the hyperbolic move out to be 6.4, giving a velocity of approximately 0.12 m/ns (representative of hard rock). Calculating the velocity and converting the two-way travel time, the distance of the void from the borehole is estimated at 10 feet, which is very close to the actual distance of approximately 12 feet. Examples and details of these processing and modeling steps with GRORADAR are presented in Olhoeft (2000).

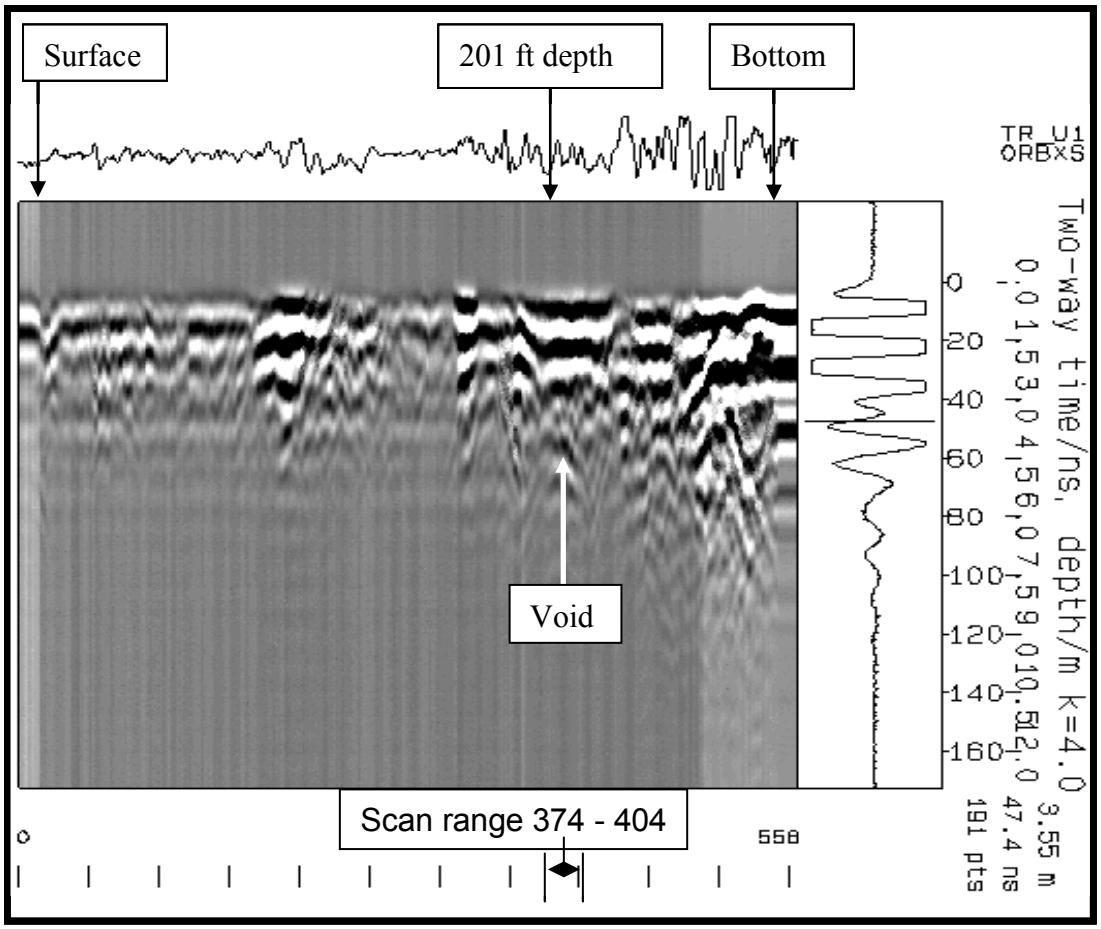

Figure 22. GPR data from Borehole U1A for the air filled void condition.

The material inside the void has an effect on the reflection signature due to the reflection coefficient at the boundary. The dielectric permittivity contrast at the void/host rock boundary causes this signature reflection. If the void is air-filled there is a polarity reversal in the reflection because the dielectric permittivity of air is lower than the host rock. Air exhibits a relative dielectric permittivity of 1.0 (normalized relative to free space). If the void is water filled, the reflection will exhibit the same polarity as the transmitted pulse. This occurs because the relative dielectric permittivity of water (approximately 81) is higher than that of the host rock (6.4).

GPR data from the water-filled void showed similar results to the air-filled void condition. Water levels in the boreholes were at a depth of approximately 200 feet during the water-filled tests, corresponding to the region where the air-filled void anomaly was interpreted. This water level is observed as the change in coupling of the GPR antenna (the lighter gray appearance of data below the water level is due to the change in antenna coupling related to the presence of water in the borehole) as illustrated in Figure 23, and suggests that the water-filled void would be at or above this water level.

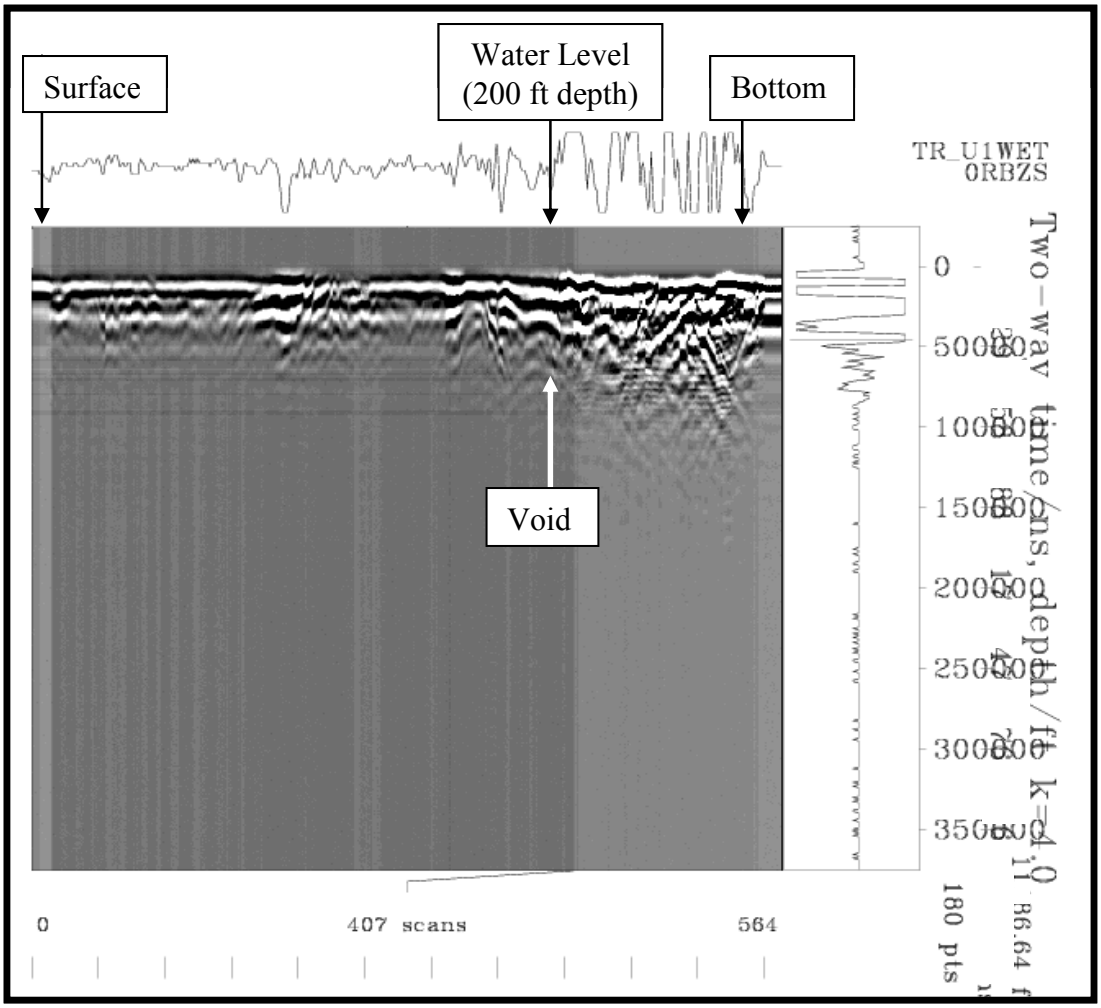

Figure 23. GPR data from Borehole U1A for the water filled void condition.

In both Figures 22 and 23, there are multiple hyperbolic features in the data that look similar to the one indicated as from the void. The asymptotic hyperbolic legs are determined by the velocity of the surrounding material which is useful in determining depth, but not otherwise useful in identifying a void. The radius of curvature at the top of the hyperbola is broader for a mine tunnel sized void as compared to that from the fractures, thus allowing the void to be distinguished and identified (and its size estimated).

5.4 Cross Hole Radar Tomography

The objective of this investigation was to conduct a cross hole radar tomography (XHRT) survey in order to map the location of the tunnel void between Boreholes U1A and U5, and to assess any variation in the dataset corresponding to air and water filled void conditions.

5.4.1 Basic Concept and Theory

The basic concept and theory of XHRT is for the most part equivalent to that of Borehole GPR, as described in Section 5.3.1 The main difference is that with XHRT, the transmitter and receiver are located in separate boreholes, and the data are interpreted using tomography inversion. The amplitude inversion will show areas between the boreholes where there are changes in the attenuation characteristics of the material between the boreholes. The travel time inversion shows areas where there are changes in the velocity of the materials between the boreholes. An important consideration is the effect of air or water filling a void on the velocity of radio energy. Water has a high dielectric permittivity which greatly slows the velocity of the radio pulse. Air has the opposite effect, increasing the velocity relative to the host rock background. As a result, travel time tomography is a useful tool for detecting both air- and water-filled voids and fractures. Dispersion is the distortion of the shape of the radio pulse as a result of attenuation and the variation of velocity with frequency. If the size of the void (and any associated fracture halo from mining activity) is comparable to the spatial wavelength of the propagating electromagnetic energy, then there will be a strong frequency dependent pulse dispersion (distortion) caused by scattering. For an air-filled void, there is an apparent velocity increase relative to the surrounding host rock, attenuation increase (due to increased conduction losses from water-filled mining induced fracturing and/or increased scattering), and increased dispersion (from scattering). For a water-filled void, there is an apparent velocity decrease, plus increased scattering and dispersion. These are all derived from the first arriving pulse wavelet energy between transmitter and receiver. If the geometry allows and there are clear diffractions present in the data beyond the first wavelet, then diffraction tomography can improve the resolution and location of a void by an order of magnitude over simple velocity or attenuation tomography alone. In practice, there are often not enough diffractions to observe or too many diffractions to sort out, so diffraction tomography is only possible in about 5 to 10% of the data. Diffraction tomography is modeling and processing very similar to migration.

5.4.2 Limitations of XHRT

The technical limitations to the use of XHRT are mostly the same as for Borehole GPR. The primary factors causing signal attenuation is the electrical conductivity of the material through which the radar energy passes and scattering. Materials with higher conductivity cause higher rates of attenuation. As discussed previously, the Edgar Mine is situated in rock with relatively low conductivity except in mineralized zones where increased attenuation results from increased fracturing, rock weathering and alteration. In addition, XHRT may be defeated by geometry even though signal may penetrate through the rock from transmitter to receiver. This occurs when there is insufficient angular spread between data sets. Unlike a hospital CAT or MRI scan, which acquires

data for 360 degrees completely around a body, borehole XHRT angular spread is limited by the length and separation of the boreholes.

5.4.3 Data Acquisition

The Army tunnel at the Edgar Mine was constructed nearly twenty years ago as a test bed for the US Army Korean Tunnel Neutralization Team (TNT). Nearly all of the associated data are classified and unavailable today. However, one example that was previously presented in public (as part of the Olhoeft, 1993, unpublished conference presentation) may be shown here for comparison.

Borehole radar systems are hard to use and few have been manufactured compared to surface GPR units (dozens compared to thousands). Finding a commercially available and suitable borehole radar was challenging. Initial calls to Mala indicated all of their units were under contract. The PEMSS system manufactured by the Southwest Research Institute for the Army Korean TNT is no longer available. Neither the GSSI nor the Sensors & Software borehole radars could go to sufficient depth.

Eventually, a RAMAC/GPR system from Mala GeoSciences became available and was employed for the Borehole XHRT. All relevant details of the data acquisition system are summarized in Section 5.3.3 of this report.

The XHRT surveys were conducted before and after the target void was filled with water. The surveys were carried out with the transmitter in one borehole while the receiver is in the other borehole. One dataset was collected with the transmitter and receiver at the same elevation ("zero offset") and moved together to continuously log up hole. Then data were collected with the transmitter offset both above and below the receiver. The offsets were 16.4 and 32.8 feet in both directions, yielding the minimum set of 5 offsets required for tomography (-32.8, -16.4, 0, +16.4 and +32.8 ft offset), and in the same fashion as data were acquired by the US Army Korean TNT. The receiver was placed in borehole U1A and the transmitter was deployed in Borehole U5. This procedure was repeated until all the data in boreholes had been acquired at the five transmitter-receiver antenna offsets. Again the radar data were examined in the field and unacceptable records were repeated until the best possible results were achieved. For the XHRT surveys, the set up was similar to the reflection method, except the transmitter and receiver were deployed in separate boreholes. As a result, two fiber optic cables with pulley tripod apparatus were used for the set up with the same distance between scans of 0.5 feet. The optical depth encoder failed during the cross hole data acquisition, and was of unique European manufacture that could not be readily replaced or repaired in the available equipment

lease window. As a result and as shown in Figure 24, antennas were then moved by hand and depths recorded from marks periodically made upon the down hole logging cable.

Figure 24. Performing hole-to-hole tomography by hand in the absence of the computer controlled winches and after depth encoder failure.

5.4.4 Data Processing and Interpretation

Because the data were acquired in the same fashion as the original US Army Korean TNT data, the same software algorithms could be used in processing and modeling (Olhoeft, 1988, 1993). The same computers and array processors are no longer available, so the software had to be ported to a modern computing environment.

This software automatically performs a series of tests on the radar data and associated information (surveying, deviation, etc.), and will not allow processing or modeling unless the data passes those tests (examples of data faults are shown in Olhoeft, 1993, which is reproduced in Appendix B). If the data pass, the first arrival time and amplitude picking and characterization of pulse distortion (for dispersion) are performed automatically. Then processing and modeling to ray path inversion of an air filled void, velocity, apparent attenuation, and dispersion tomography, and if possible diffraction tomography are also all automatically performed (Olhoeft, 1993). An excellent introductory discussion of the electromagnetic character of void (tunnel) anomalies in hole-to-hole radar data may be found in Griffin et al. (1988).

Unfortunately, the data sets acquired at the Edgar Mine fail a key test, and processing to tomograms and further full waveform modeling are not possible. Note that such processing may be done, but it will result in artifacts and inaccuracies that will be misleading.

Figures 25, 26 and 27 show one of the datasets acquired along this same Army tunnel after it was first created, nearly 20 years ago. These are not in the same boreholes but a nearby pair (we are prohibited from stating specific locations for any of this data, which also prevents us from showing the same hole pair) which show a similar response. These were acquired using the PEMMS II borehole radar tomography system. These figures are in the same format as the figures in Olhoeft (1988, 1993), as reproduced in Appendix B.

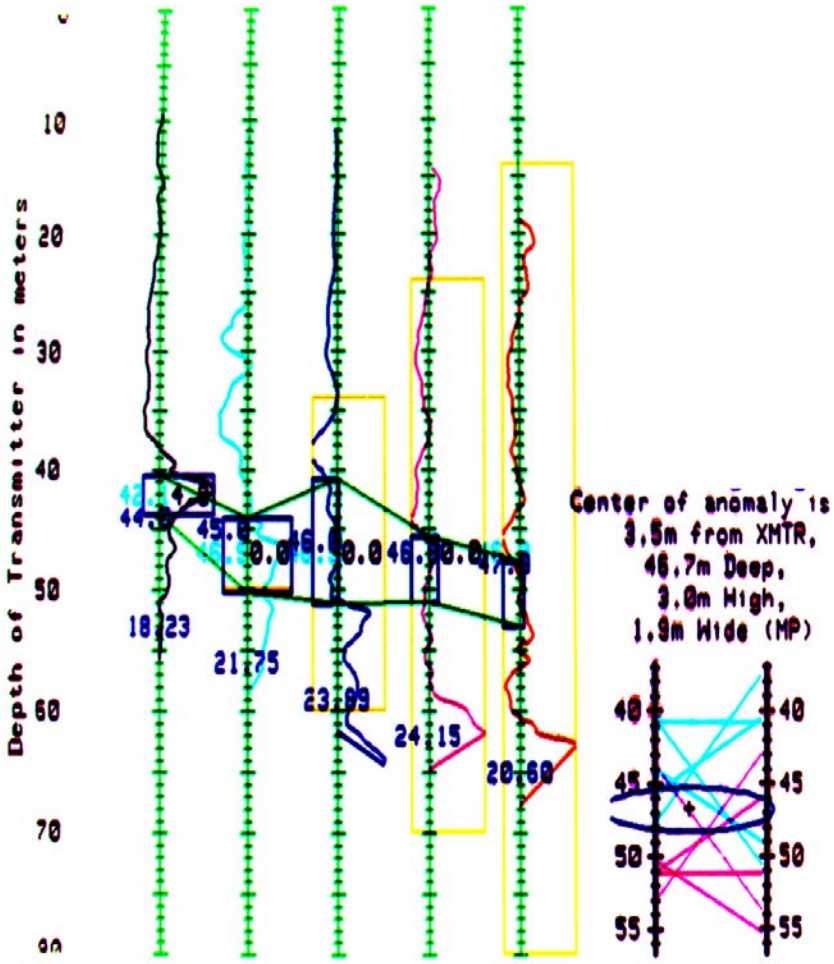

Figure 25. Original PEMSS data of nearly 20 years ago along the Edgar Mine Army Tunnel in the same format as Figures 5 and 7 in Olhoeft (1988) and 2 and 6 in Olhoeft (1993) (see Appendix B). The radar data are plotted as a product of velocity and apparent dispersion (black, cyan, blue, pink, red lines) at five transmitter receiver offsets (vertical green axis lines at (left to right) +10, +5, 0, -5 and -10 m T-R offsets), with the automatic selection of the most probable air-filled void on the basis of the maximum anomaly amplitude in each offset. The blue boxes are the most likely anomaly set which lies within the possible range correlated from offset to offset and limited by the antenna pattern (yellow boxes). On the right is the ray path inversion to locate the void between the boreholes, with the most likely (plus sign) and locus of possible void locations (blue ellipse) shown. This is a reproduction of a 1990 vintage scanned slide, which was presented at a public conference and is all that may be reproduced today (and only if the precise locations of the boreholes are not given). The slide was originally taken with a camera viewing the curved surface of a CRT, and so exhibits some barrel and other distortions which the author has only partially been able to compensate.

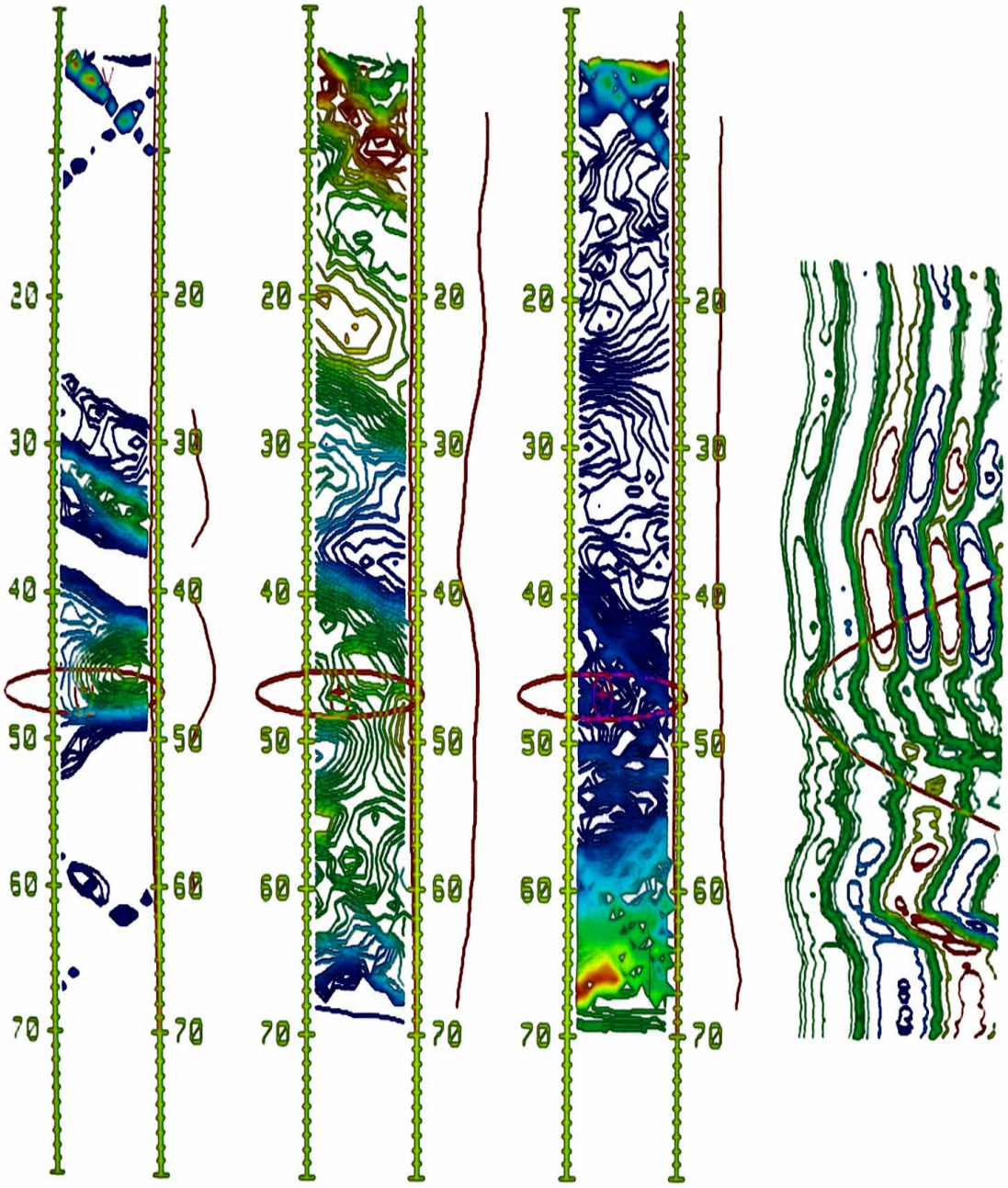

Figure 26. From left to right, velocity, apparent attenuation and dispersion tomographs, and a crude diffraction model attempt to fit the data on the right, in similar format to Figures 6 and 8 in Olhoeft (1988) and Figures 3 and 7 in Olhoeft (1993) (see Appendix B). The air filled void is hard to see in the tomograms until the scale is changed (see Figure 27). For a better illustration of the diffraction modeling, see Figures 4 and 8 in Olhoeft (1993) (see Appendix B).

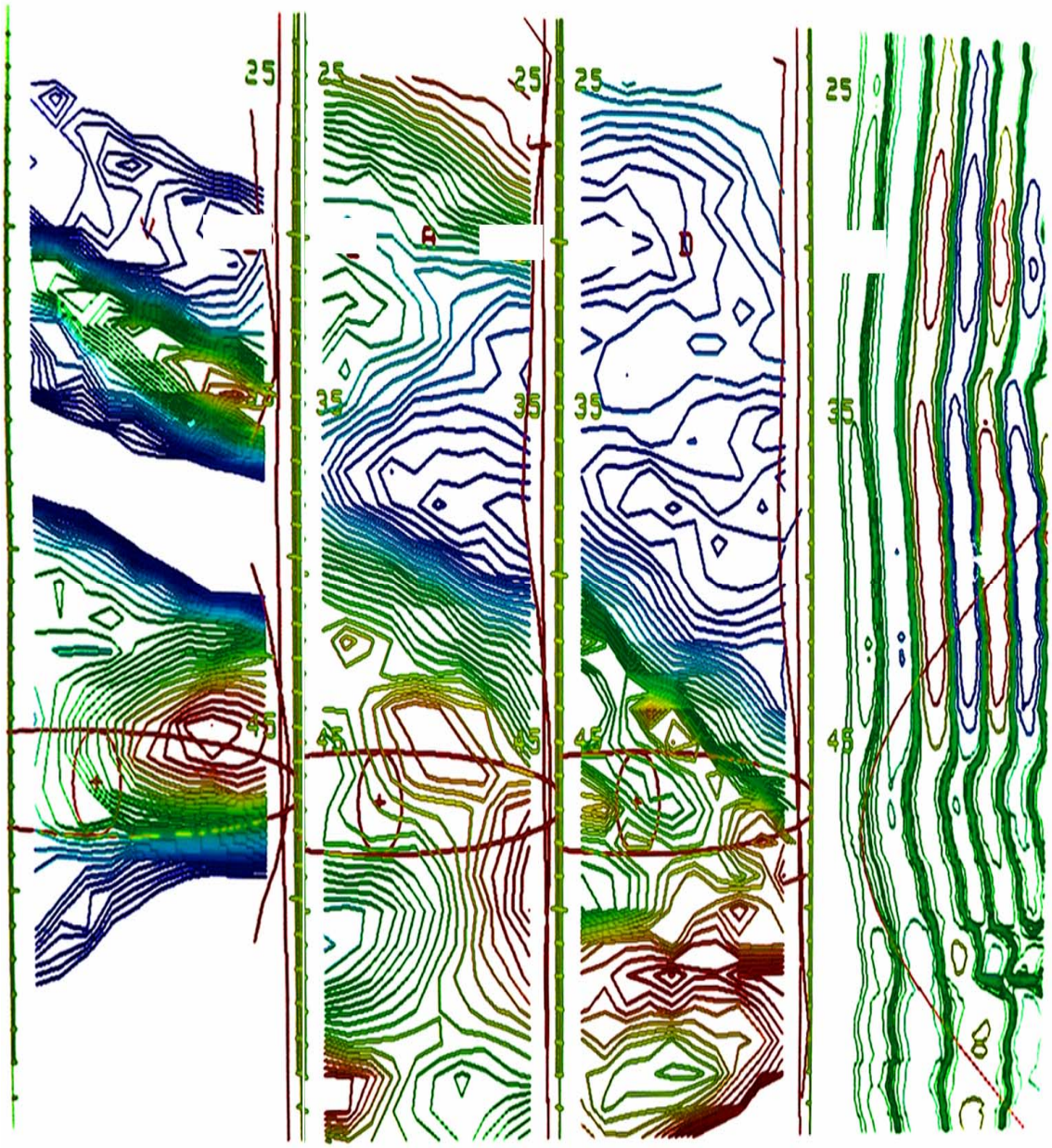

Figure 27. With a scale change, the air filled void becomes easier to see (the red contour coincident anomalies in the velocity and attenuation tomographs, though the automatic tunnel detection algorithm successfully located it anyway). Note that the automatic ray path inversion (the two red ellipses in each tomograph) is slightly off as the automatic algorithm chose the wrong anomaly in the level run. The smaller red ellipse is the estimated size and shape of the tunnel, while the larger ellipse is the locus of possible locations.

Figure 28 shows the data acquired for the current project with the Mala RAMAC system, illustrating the problems. The upper set of grey scale images are with the air-filled tunnel and the lower are with the water-filled tunnel. The red boxes overlain in each offset between transmitter and receiver project on the basis of the old PEMSS data where the tunnel void should appear.

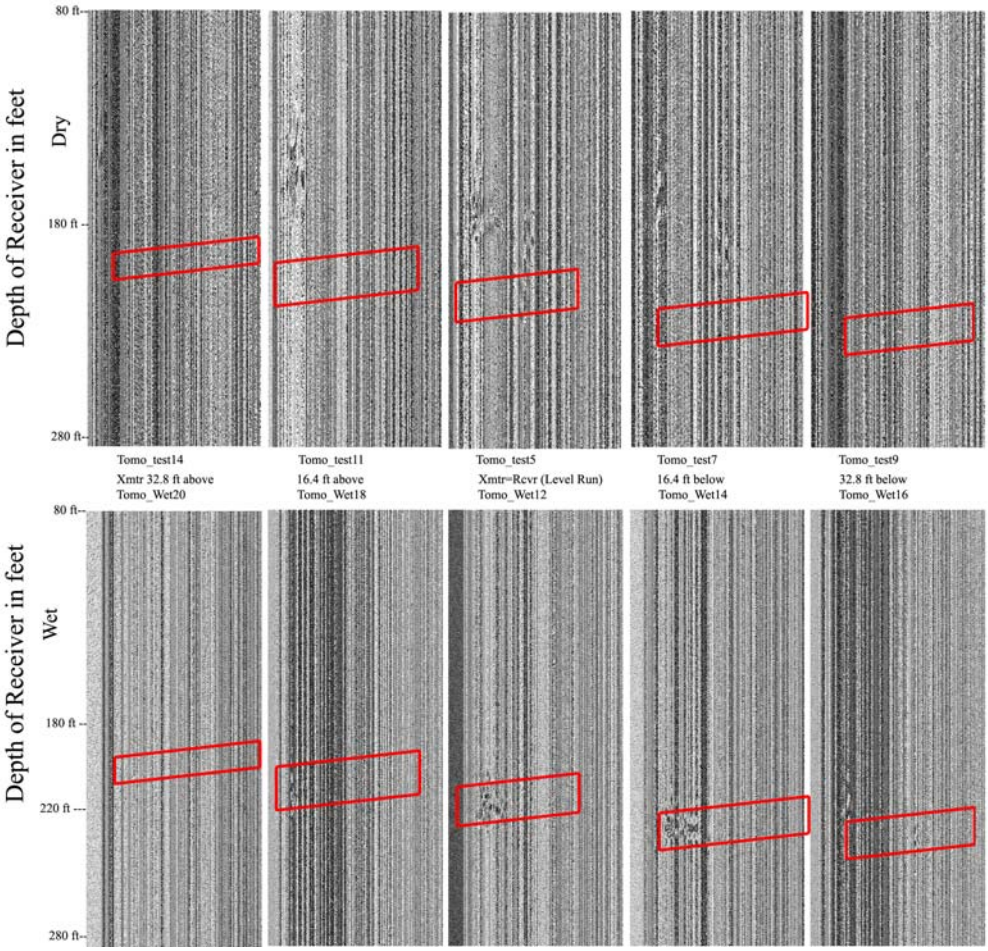

Figure 28. The red boxes show the expected amplitudes (horizontal box width) and depths (vertical box height) of the air- and water-filled voids in the current RAMAC datasets projected from the nearly 20 year old PEMSS data (see text for extended discussion).

The vertical banding in the data is caused by poor coupling between the radar antennas and the rock formation, and was also seen in the PEMSS data (see contours in rightmost panel of Figures 26 and 27). In the wet data, there is a radar response within the expected zone clearly evident in two (0 and 16.4 ft below) of the five offsets, possibly in a third (16.4 ft above), but only imagined in 32.8 ft below and not at all visible in 32.8 ft above. Without five offsets, the tomography cannot be performed. However, the RAMAC did locate the depth of the tunnel void correctly in the zero offset level run. The other offsets

are required to locate the tunnel position between the holes, and to estimate the void size and shape. For each red box, the vertical extent indicates the projected depth and the horizontal width the relative amplitude across the offsets as expected by the PEMMS system. It is not known why the RAMAC system did not measure the same amplitudes. No operator errors were observed, so the difference must lie within the radar hardware (perhaps dynamic range, filtering, or antenna pattern).

The dry data exhibit the same problem plus an additional issue. These data were not acquired in exactly the same fashion as the wet data (see Observer Notes in Appendix A). They have been transformed here to look the same for comparison. Note that there are clear radar responses to the air filled void in three of the five offsets, but no observable response in the largest two offsets, so tomography again cannot proceed. Note also, that the responses are in the wrong locations in depth, and the 16.4 ft below offset response is also inconsistent with the zero offset level run and the 16.4 ft above offset trend. The data acquisition system was noted to have problems with the depth encoder during the acquisition of these data, which is an explanation that fits with these depth problems.

6.0 DISCUSSION AND CONCLUSIONS

6.1 Cross Hole Seismic Tomography

The low velocity anomalies interpreted as the target void are located above the known void elevation, with vertical offsets ranging from about 3 to 8 feet. These differences, in part, may be due to the irregular shape of the void and fractures around the void walls, or due to the effects of the tomographic inversion algorithm and gridding. Additionally, there may be a small error in the measured depth of the source and receiver string. The source and receiver string depths were measured by attaching a fiberglass tape measure to the each string. It is possible that the tape measure could slide, but this is likely to be less than 1.0 foot in error. In the air filled and water filled tomograms, there are low velocity zones above the true void depth, which may be due to the presence of fracturing/loosening within the rock mass as a result of the tunnel driving. However, it appears from both the raw seismic records and the final tomograms that the data quality acquired with the water-filled void was better than that of the air-filled void. This may result from increased saturation of the fractures within the rock due to water leakage from the void. This may also be attributed to decreased signal scattering from the void/rock interface due to the lower acoustic impedance between water/rock versus air/rock boundary. Additionally, saturated fractures between the boreholes may have reduced signal attenuation, providing for higher signal-to-noise ratio data and higher frequency content.

The results of the survey indicate that the presence of the void could be detected using XHST under both air filled and water filled conditions. In both cases, a low velocity zone was present between the boreholes that correlated reasonably well with the location of the known void. Other low velocity zones were present above the void, which may indicate the presence of fracturing/loosening within the rock mass. When the boreholes were filled with water, there was significant leakage from the boreholes indicating that open fractures are present in this area.

Other conclusions drawn from the data include:

- Reacquiring the data using a sparker versus the swept frequency Etrema source provided significantly better data quality. It appears that there was significant cross-talk between the source input signal and the receivers, that was not evident in the uncorrelated field records during the Etrema data acquisition.

- The use of the new 24-channel hydrophone string provided improved signal-to-noise content than the 12-channel string used in the earlier data collection.

- The void was detectable when both air filled and water filled; however, it appears that the data quality was higher with the water-filled void.

In general, the XHST technology was successful in detecting the location of the void at this site. Had detailed borehole logs been available, inhomogeneities in the rock mass

may have become apparent, and modeling of such inhomogeneities may have result in improved accuracy of the results.

6.2 Borehole Radar

The air- and water-filled borehole GPR surveys were able to detect the presence and location of the target void. Although data appear different (because the GPR range was doubled from 200 ns in the dry tests to 400 ns in the wet), the anomaly associated with the void appeared at the same range or distance from the borehole of approximately10 feet. The higher range results in the reflections near the borehole appear to be compressed relative to the dry tests.

The void was objectively identified amongst similar looking hyperbolas by the pulse polarity reversal between the (dry) air-filled to (wet) water-filled, and the broader (greater radius of curvature) character of the peak in the hyperbola.

6.3 Cross Hole Radar Tomography

The commercially available Mala RAMAC cross hole radar system (the only such system in current production) did not acquire data suitable for tomography in the environment of the Edgar Mine Army Tunnel. Both the air-filled and the water-filled void radar data had sufficient anomaly amplitude and dynamic range in too few transmitter-receiver offsets to proceed with tomographic processing and modeling. Further, the acquisition of the radar data for the air-filled void also had depth location errors inconsistent across the three offsets that did have adequate anomalies.

By comparing the figures in Olhoeft (1988, 1993), reproduced in Appendix B, with those in this report, it can be noted that the Edgar Mine site is a very difficult site for radar based void imaging. The data at the Edgar Mine have more loss and noise than those presented in Olhoeft (1988, 1993), resulting from mineralized fracture zones and consequent increased electrical conduction losses and scattering. The more than 20 year old PEMSS borehole radar worked better than the more recent vintage commercially available system. There are several possible reasons for this: the failure of the encoder and loss of accurate encoder-based depth locations for the antennas, higher power or higher system dynamic range in the PEMSS over the RAMAC system (speculation as the specifications are unknown and considered proprietary), differing antenna patterns between the systems, differing antenna-ground coupling, and higher electromagnetic loss at the Edgar Mine site (due to local weather or climate induced changes in moisture content) over time, or changes in the Mine site character (increased fracturing for example) caused by the intervening 20 years of continued mining and tunnel development.

The data acquired nearly 20 years ago confirm that hole-to-hole or cross-hole radar can detect and locate air- or water-filled mine tunnel voids. Unfortunately, although uncertain at the time of our proposal, the commercially available systems of today do not replicate that ability. Thus, CSM was unable to effectively demonstrate the efficacy of cross-hole radar to MSHA and the mining industry.

The 20 year old PEMSSII hole-to-hole radar system was specifically engineered for the Korean Tunnel Detection Program of the U.S. Army. No modern system exists with comparable hardware specifications, nor are the currently available commercial systems designed solely for void detection. The currently available commercial systems also do not have the dedicated tunnel detection software (though the software is available). The PEMSSII system demonstrated the ability of cross hole radar to locate air filled voids in Korea, and use automatic software data processing, display and interpretation to determine both depth and location between boreholes, and to estimate the void size, shape, and material filling (Olhoeft, 1988, 1993). Of the three major GPR manufacturer's commercially available borehole radar systems: none meet intrinsic safety requirements for use in mines, Sensors & Software's borehole radar has shallow depth limits on the cabling that prevent effective use in normal coal mine situations; GSSI's borehole radar system is not waterproof (though users have modified it to be useable in water filled holes) and has cable depth limits; and we have just demonstrated that the Mala system does not perform as well as PEMSSII did (for several possible reasons stated earlier).

There is no technical reason preventing a PEMSSII type borehole radar system from being developed and used for void detection. However, there must be economic demand for such a commercial system to give the manufacturers incentive to continue production. Nearly 20 years ago, there was a commercial manufacturer of a radar that met intrinsically safe Class II Divison 1 Group F combustible coal dust requirements in an MSHA certified explosion proof housing, Xadar Inc. However, both limited regulatory requirements for its use and inadequate market demand for the product ended that business. Today's commercial GPR manufacturers also need to deal with a new FCC regulatory environment that did not exist 20 years ago, further increasing their costs for deployment of new radar hardware. The FCC only regulates the electromagnetic spectrum in air, not underground, so two modes of radar operation would be required: a low power FCC certified mode for use above ground in hole-to-hole calibration, and a higher powered mode that could only be used once the tool was underground.

7.0 REFERENCES

Glass, K.B., Duff, B.M., Converse, M.E., King, D.E., and King, J.E., 1988, The development of a pre-prototype pulsed electromagnetic search system (PEMSS-II): SouthWest Research Institute Final Report, Contract DAAK70-86-C-0093 to U.S.Army Belvoir Research Development and Engineering Center, VA, var.pag.

Griffin, J.N., Meade, J.L., and Kemerait, R.C., 1988, Overview of the PEMSSII Signal Processing System: Ensco report DCS-SFG-88-93, in appendix A to Glass et al. (1988).

Lytle, R.J., K.A. Dines, E.E. Laine, and D.L. Lager, 1978, Electromagnetic Cross-Borehole Survey of a Site Proposed for an Urban Transit Station. UCRL-52484, Lawrence Livermore Laboratory, University of California, 19 pp.

Olhoeft, G.R., 1988, Interpretation of hole-to-hole radar measurements, in Proceedings of the Third Technical Symposium on Tunnel Detection, January 12-15, 1988, Golden, CO, p. 616-629.

Olhoeft, G.R., 1993, Velocity, attenuation, dispersion and diffraction hole-to-hole radar processing, in Proceedings of the Fourth Tunnel Detection Symposium on Subsurface Exploration Technology, Colorado School of Mines, Golden, CO, 26-29 April 1993, Miller, R., ed.: U.S. Army Belvoir Research, Development and Engineering Center, p. 309-322.

Olhoeft, G. R., 2000, Maximizing the information return from ground penetrating radar: J. Appl. Geophys., v. 43/2-4, p. 175-187.

Peterson, J.E., B.N. Paulson and T.V. McEvilly, 1985, Applications of Algebraic Reconstruction Techniques to Cross hole Seismic Data. Geophysics, v. 50, pp. 1566-1580.

APPENDIX A – Observer Notes- XHRT

MSHA/CSM Observer Notes
Edgar Mine, Idaho Springs, CO, air-filled void

All tomography (Tomo_) collected with 100 MHz borehole antennas:

1. start with tools at the bottom of the whole
2. Receiver is in Borehole U1A
3. Transmitter is in Borehole U5
4. Offsets are applied to transmitter relative to receiver
5. Last trace is air wave.

File name	Start	End	Offset (ft)	Comment	Distance between scans (ft)	Range (ns)	No. of traces	File time stamp
Tomo_test2	282	80	0	Level run	0.5	200	406	1:07
Tomo_test5	282	80	0	Repeat	0.5	200	407	1:22
Tomo-test7	282	0	-16.4	Tx below Rec.	0.5	200	593	1:36
Tomo_test9	282	80	-32.8	Tx below Rec.	0.5	200	408	1:47
Tomo-test11	282	80	16.4	Tx above Rec.	0.5	200	407	1:55
Tomo_test14	282	80	32.8	Tx above Rec.	0.5	200	407	2:07
TR_U1	0	~270	9	Profile in Borehole U1A	0.5	200	556	2:46
TR_U5	0	~300	9	Profile in Borehole U5	0.5	200	608	2:54

MSHA/CSM Observer Notes
Edgar Mine, Idaho Springs, CO, water-filled void

All tomography (Tomo_) collected with 100 MHz borehole antennas:

6. start with tools at the bottom of the whole
7. Receiver is in Borehole U1A
8. Transmitter is in Borehole U5
9. Offsets are applied to transmitter relative to receiver
10. Last trace is air wave.
11. Range is doubled to 400ns
12. No. of samples is doubled to 1024

File name	Start	End	Offset (ft)	Comment	Distance between scans (ft)	Range (ns)	No. of traces	File time stamp
Tomo_Wet12	282	80	0	Level run	0.5	400	410	2:10
Tomo_Wet14	282	80	-16.4	Tx below Rec.	0.5	400	410	2:18
Tomo-Wet16	282	80	-32.8	Tx below Rec.	0.5	400	411	2:28
Tomo_Wet18	282	80	16.4	Tx above Rec.	0.5	400	411	2:36
Tomo_Wet20	282	80	32.8	Tx above Rec.	0.5	400	412	2:44
TomoM125a	0	275	125	Tx only moved	0.5	400	554	3:11
TomoM140	125	275	140	Tx only moved	0.5	400	306	3:14
TomoM155	125	275	155	Tx only moved	0.5	400	305	3:20
TomoM1170	125	275	170	Tx only moved	0.5	400	305	3:23
TomoM180	125	275	185	Tx only moved	0.5	400	303	3:26
TomoM200	125	275	200	Tx only moved	0.5	400	304	3:32
TomoM215	125	275	215	Tx only moved	0.5	400	305	3:38
TomoM230	125	275	230	Tx only moved	0.5	400	306	3:40
TomoM245	125	275	245	Tx only moved	0.5	400	307	3:42
TomoM260	125	275	260	Tx only	0.5	400	305	3:45

				moved				
TomoM275	125	275	275	Tx only moved	0.5	400	308	3:52
TR_U1	0	~270	9	Profile in Borehole U1A	0.5	200	564	4:51
TR_U5Wet	0	~300	9	Profile in BH U5	0.5	200	618	4:38

APPENDIX B – Reprints of Olhoeft (1988 & 1993)

Olhoeft, G.R., 1988, Interpretation of hole-to-hole radar measurements: in Proc. of the Third Tech. Symp. on Tunnel Detection, January 12-15, 1988, Golden, CO, p. 616-629.

Interpretation of hole-to-hole radar measurements

by

Gary R. Olhoeft
U. S. Geological Survey
P. O. Box 25046 DFC MS964
Denver, CO 80225-0046

Abstract

Time-domain electromagnetic propagation measurements between two boreholes yield several kinds of information about the media between the holes. The ray-path distance divided by the first-arrival-time is average velocity. The reciprocal of the product of first-arrival amplitude times ray-path distance is proportional to attenuation. The change in shape of the wavelet is a measure of dispersion. Dispersion is the change in frequency content of the wavelet during propagation. The velocity primarily represents changes in bulk density and water content. The attenuation primarily represents changes in fracture density and water content. The dispersion primarily represents changes in scattering. Back projection reconstruction techniques allow tomographic velocity, attenuation and dispersion contour sections to be produced. Increased fracture density appears as increased attenuation and decreased velocity (for water-filled fractures) with little or no change in dispersion. The presence of an air-filled mine tunnel appears as an increase in velocity, attenuation, and dispersion. The tunnel also produces multiple reflection and multipathing interference and diffraction effects. However, none of these effects are by themselves good indicators of the presence of a tunnel as they may also come from various features in normal geology. It is the coincidence of several of the effects that indicates a tunnel may be present. Limited offset angles effectively limit the ability of tomographic reconstruction in locating 2 meter diameter air-filled mine tunnels to borehole separations of less than 30 meters.

Presented at the Third Technical Symposium on Tunnel Detection, Golden, Colorado, January 12-15, 1988.

Interpretation of hole-to-hole radar measurements

by Gary R. Olhoeft

PEMSS (Pulsed Electromagnetic Search System), manufactured by the Southwest Research Institute, is a radio-frequency, short-pulse, time-domain radar system (Owen, 1981; Duff, 1988). It is operated with a transmitter in one borehole and a receiver in another borehole for hole-to-hole propagation measurements. The transmitter and receiver are both moved upward at constant and equal rates while measurements are recorded. The transmitter may be at the same depth in the first hole as the receiver in the second hole, or there may be an offset in depth between the two. The data discussed in this paper were acquired with the receiver 10 meters below, 5 meters below, at the same level, 5 meters above and 10 meters above the transmitter.

As seen in Figure 1 for a few representative offsets and measurement points, such multiple offsets provide several different geometries of measurement for each point in the ground between the two boreholes. Tomographic reconstruction techniques (Natterer, 1986) allow these multiple measurements to be reconstructed as cross-sections of the variation in properties between the two holes.

Figure 2 illustrates a typical PEMSS measurement of received electromagnetic energy versus time after transmission. A record like this is produced every 0.2 meters in depth at each offset. It is parameterized as shown in Figure 2 in terms of first-arrival time, amplitude and dispersion (as dominant period) using an automatic first-arrival picker. For low amplitude signals, a deconvolution statistical picker is used to locate and parameterize the received signal. In Figure 3, the solid line is a low amplitude original wavelet on the same scale as Figure 2, and the dashed line is the deconvolution-filter-enhanced wavelet. The enhanced wavelet is used to locate and focus the search for the first-arrival parameters in the original wavelet.

The wavelet dispersion parameter in Figures 2 and 3 is an approximate measure of the true dispersion in the wavelet. The rock through which the electromagnetic energy propagates acts like a bandpass filter. The loss tangent in Figure 4 is a measure of attenuation of the electromagnetic energy. The lower curve labelled 'granite' represents a typical electromagnetic loss for one to two percent water in microfractures over an average distribution of scale lengths for medium grained granite. The curve represents the shape of a band-pass filter. The lower frequency bound is the finite DC conduction loss. The upper frequency bound is the dielectric relaxation loss in water plus electromagnetic

An air filled mine tunnel appears as a velocity high (air has higher electromagnetic velocity than rock), an attenuation high (from increased fracture conductivity and scattering losses) and a dispersion high (tunnel scattering changing filter shape versus frequency). Attenuation alone can be higher due to increased fracturing or faulting, mineralized zones (clay or graphite) or increased water content. These effects will decrease velocity and may not alter dispersion (depending more upon scale). Thus, the product of velocity times dispersion is a good first indicator of the presence of an air-filled void. The upper right portion of Figure 5 illustrates this product as logs for the five offsets. The lower right portion shows the resultant ray-trace inversion of the largest anomaly. This solution shows an anomaly of about tunnel size at 89.7 meters deep and 11.3 meters from the transmitter hole.

The original waveform data (as in Figures 2 and 3) also exhibit hyperbolic diffraction patterns due to the presence of the tunnel. However, these diffraction patterns are indistinguishable from those due to faults in complicated geology. The dispersion effect may appear due to similar sized geological features which produce similar scattering or multipathing effects. The velocity change may be produced by a lower density material. The attenuation change may be produced by a change in resistivity or fracturing. Thus, there are no unique tunnel indicators. However, the coincidence of several of these indicators should be worthy of investigation.

The velocity, attenuation and dispersion logs for each of the five offsets are run through a back-projection tomographic reconstruction algorithm and plotted as the cross-sections in Figure 6. The data are plotted in the unwrapped plane between the two holes and relative to the transmitter hole. The black line running up the right side of each section is the location of the receiver hole relative to the transmitter hole at the left side. All three cross sections are scaled from low to high values as blue to green to yellow to red. The black circle is the ray-path inversion of Figure 5. Note that this is the location of a velocity high, an attenuation high and a dispersion high. This is also the location of a known 2-meter diameter air-filled mine tunnel. The other variations shown in the cross section represent changes in the geology between the two holes, primarily changes in the fracturing of the granite.

Figures 7 and 8 illustrate the data from the same known tunnel further along its length in a more complicated environment. This shows the tunnel as being within the lower of two fault planes. The two faults are attenuation highs but velocity lows due to their higher water content compared to the surrounding rock. Note that the tunnel

location in the ray path inversion is not as accurate as the previous figure and that the tomographic cross sections are required to show the context (within the lower of two faults). It is doubtful that this tunnel could be found with only one of the parameters (velocity, attenuation or dispersion). The coincidence of the anomalies in all three parameters clearly shows the presence of the tunnel despite the complicating geological features.

The PEMSS system acquires approximately 1.5 megabytes of data per hundred meters of hole-pair. It takes a Hewlett Packard HP-9000/520 computer running Rocky Mountain BASIC 2.0 approximately 8 hours to process the data into the form shown in Figures 5-8. With the addition of an Analogic AP-500 array processor, the time is reduced to about 20 minutes (most of which is plotting time).

There are several electromagnetic hole-to-hole radar systems in use around the world. Between them, they have demonstrated depth penetrations of tens to hundreds of meters through granite and kilometers through salt and polar ice. However, no electromagnetic system can penetrate more than a meter or two through highly conductive materials such as graphite, sulfide ores, salt water or clay. Further, the mathematics of tomographic reconstruction become untenable with limited angles of offset (see demonstration in Natterer, 1986).

Using offsets of plus and minus ten meters with holes 20 meters apart produces maximum offset angles of 26.6 degrees. In relatively clean geology, this results in anomaly location uncertainties of about 2 meters both horizontally and vertically (see Figure 6). In complex geology, both resolutions deteriorate (Figure 8). With the same offsets at greater hole separation, the vertical resolution remains about the same, but the horizontal resolution deteriorates with the decreasing offset angle. At 36 meter borehole separation with 10 meter offsets, the angle reduces to 15.5 degrees and the horizontal uncertainty deteriorates to 20 meters. The ability to acquire larger offsets is limited by the ability of the system to penetrate greater distances (sometimes) and the length of the borehole (more often). The size of the anomaly also decreases with increasing borehole separation (a 2 meter air-filled void is a smaller velocity change in 20 versus 16 meters of rock, see Figures 5 and 7).

Thus, using hole-to-hole electromagnetic propagation for the detection of 2 meter diameter air-filled tunnels is effectively limited to about 30 meter hole separations under ideal conditions. Increased geologic complexity or the presence of increased electromagnetic losses (such as conductive clay or excessive fracture scattering) could further reduce this effective distance.

Acknowledgement

This work was funded by the U.S. Army Belvoir Research, Development and Engineering Center, Ft. Belvoir, Virginia.

References

Duff, R., 1988, Short pulse hole-to-hole electromagnetic tunnel detection system and signal processing development, Proceedings of the Third Technical Symposium on Tunnel Detection, Golden, Colorado, January 12-15, 1988, this volume.

Natterer, F., 1986, The mathematics of computerized tomography, NY, Wiley, 222p.

Owen, T. R., Cavity detection using VHF hole-to-hole electromagnetic techniques, Symposium on tunnel detection, Colorado School of Mines, Golden, Colorado, July 21-23, 1981, U.S.Army MERADCOM, Ft.Belvoir, VA, p.126-141.

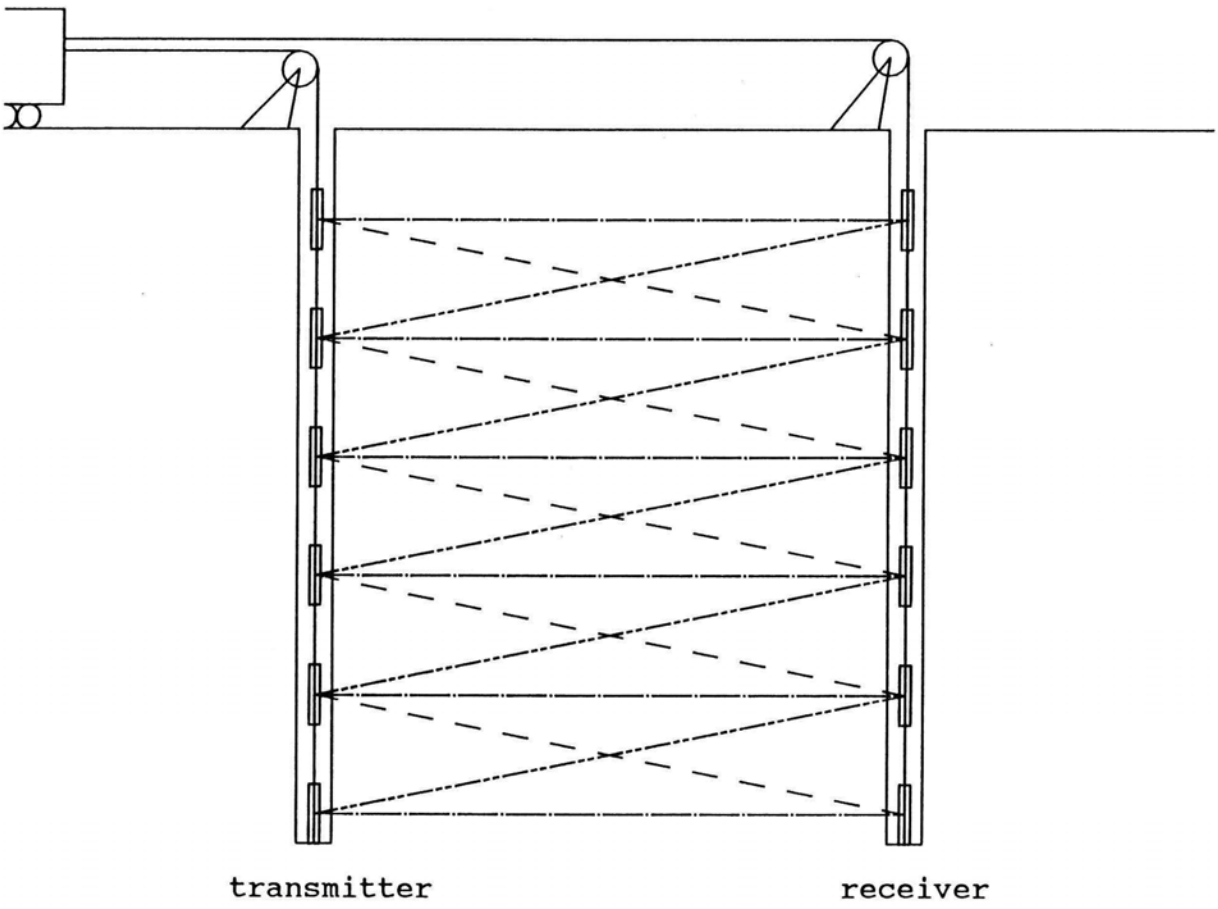

Figure 1 - The geometry of hole-to-hole tomography. The level path is that with zero offset (dot-dash line). The transmitter above the receiver offset is the dashed line. The transmitter below the receiver is the dot-dot-dash line. Both transmitter and receiver are moved up the hole at the same speed. Only a few measurement points, offsets and raypaths are shown. Typically, the holes are not straight, requiring measurement of hole deviation to correct raypaths and tomographic reconstruction.

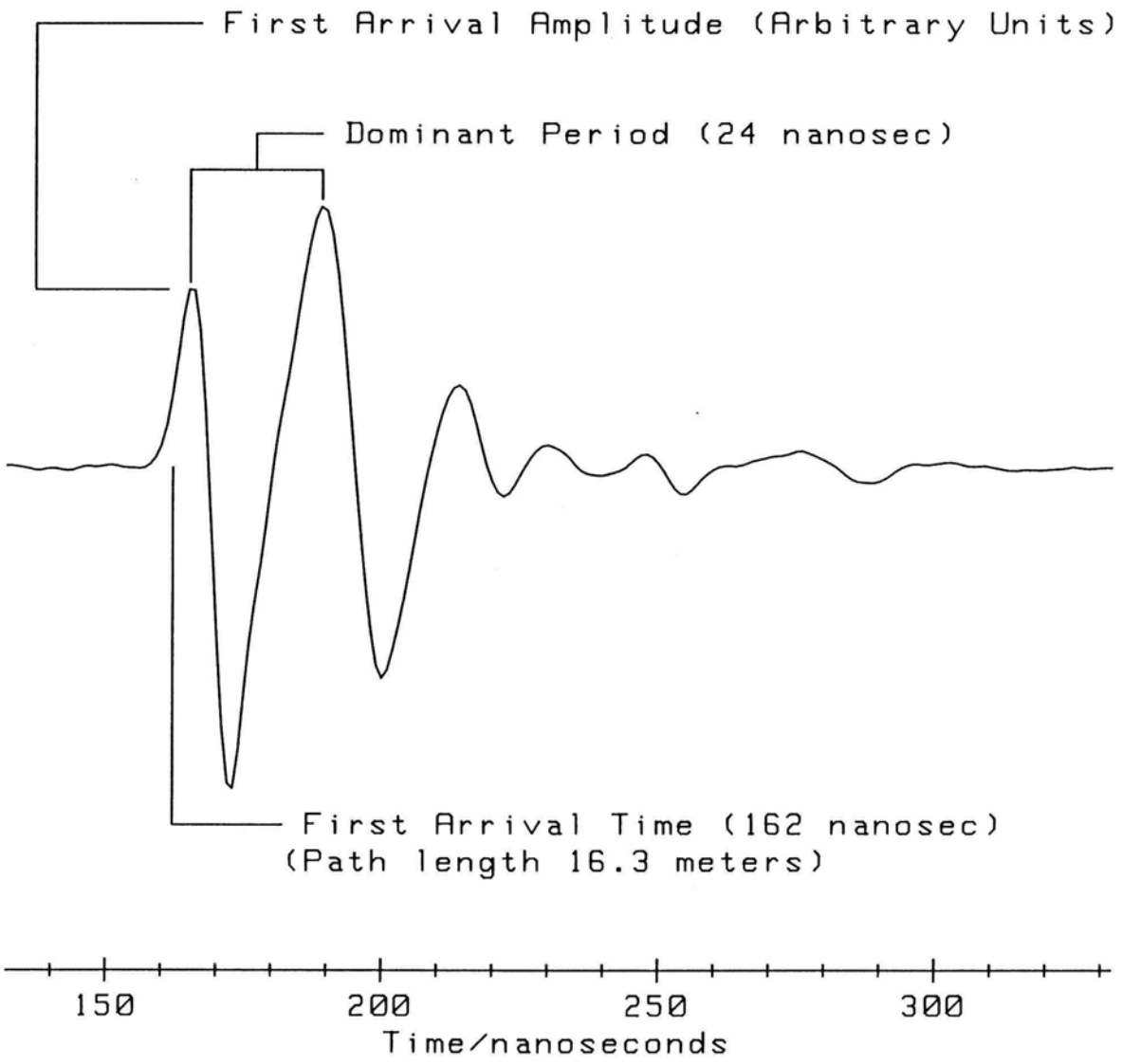

Figure 2 - A typical received wavelet in normal granite with parameterization as shown. Time is relative to transmitter. Dominant period is used to approximate dispersion.

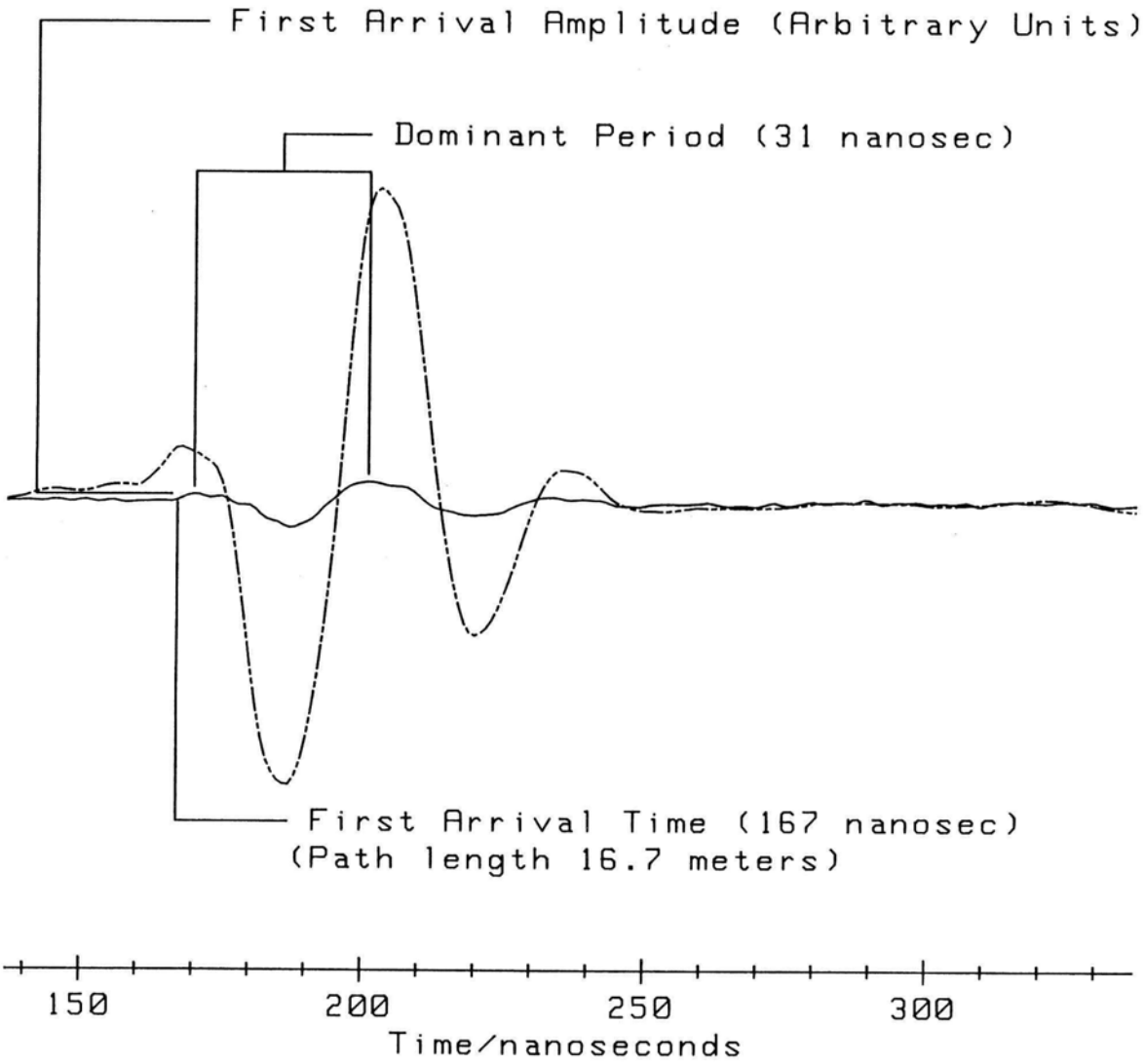

Figure 3 - A typical low-amplitude received wavelet in granite through a tunnel with parameterization as shown. The vertical scale is the same as Figure 2. The dashed line is after deconvolution enhancement (see text).

Figure 4 - The change in loss tangent (proportional to attenuation) versus frequency for 'typical' granite with and without a two meter diameter tunnel. Both curves include the losses from DC conduction and scattering in one to two percent water saturated microfractures and a typical medium-grained granite distribution of scale lengths. The 'tunnel' curve adds the conductivity and scattering effects for the slightly increased water content of a two meter diameter tunnel with its associated halo of stress-induced fractures.

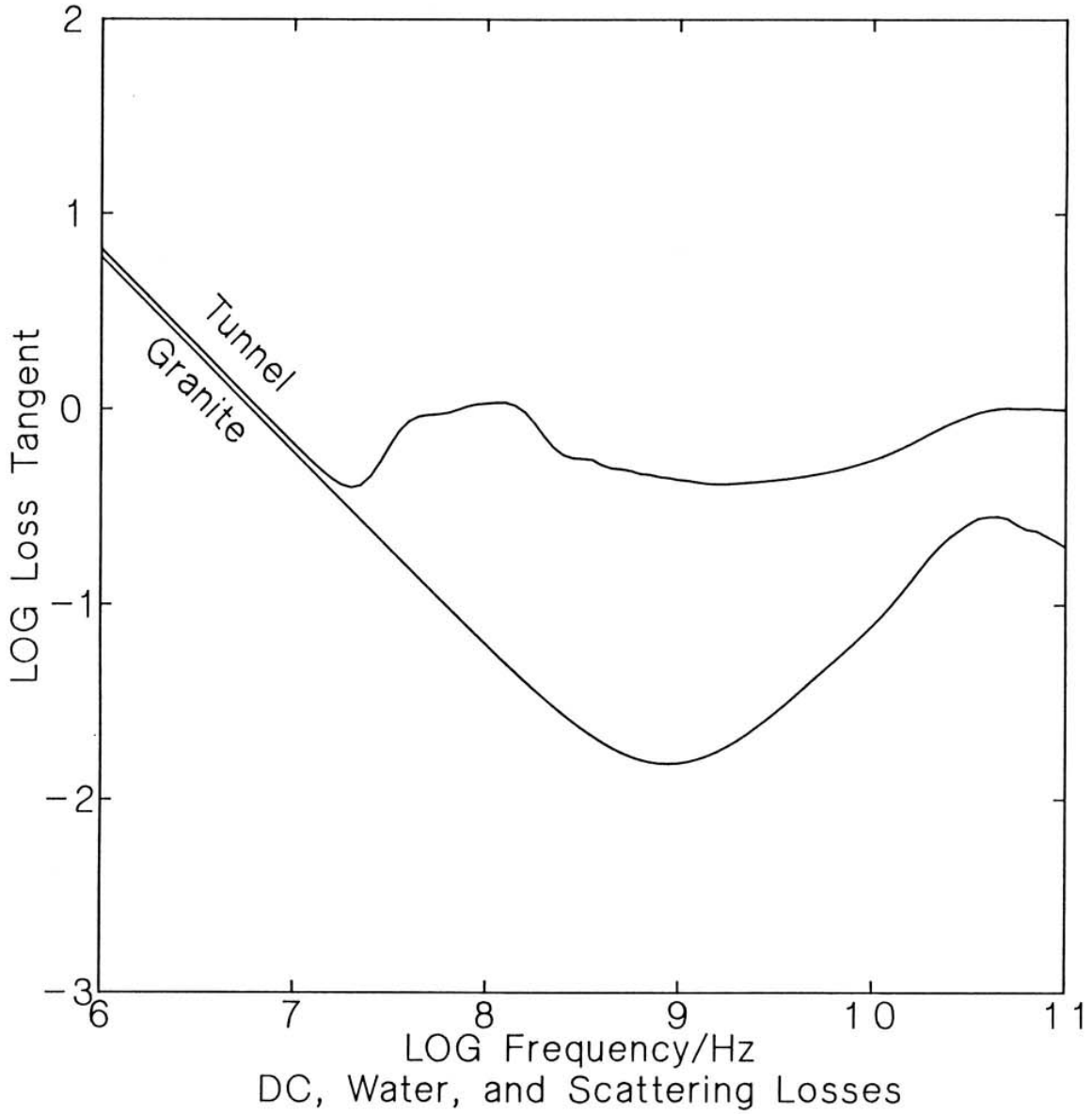

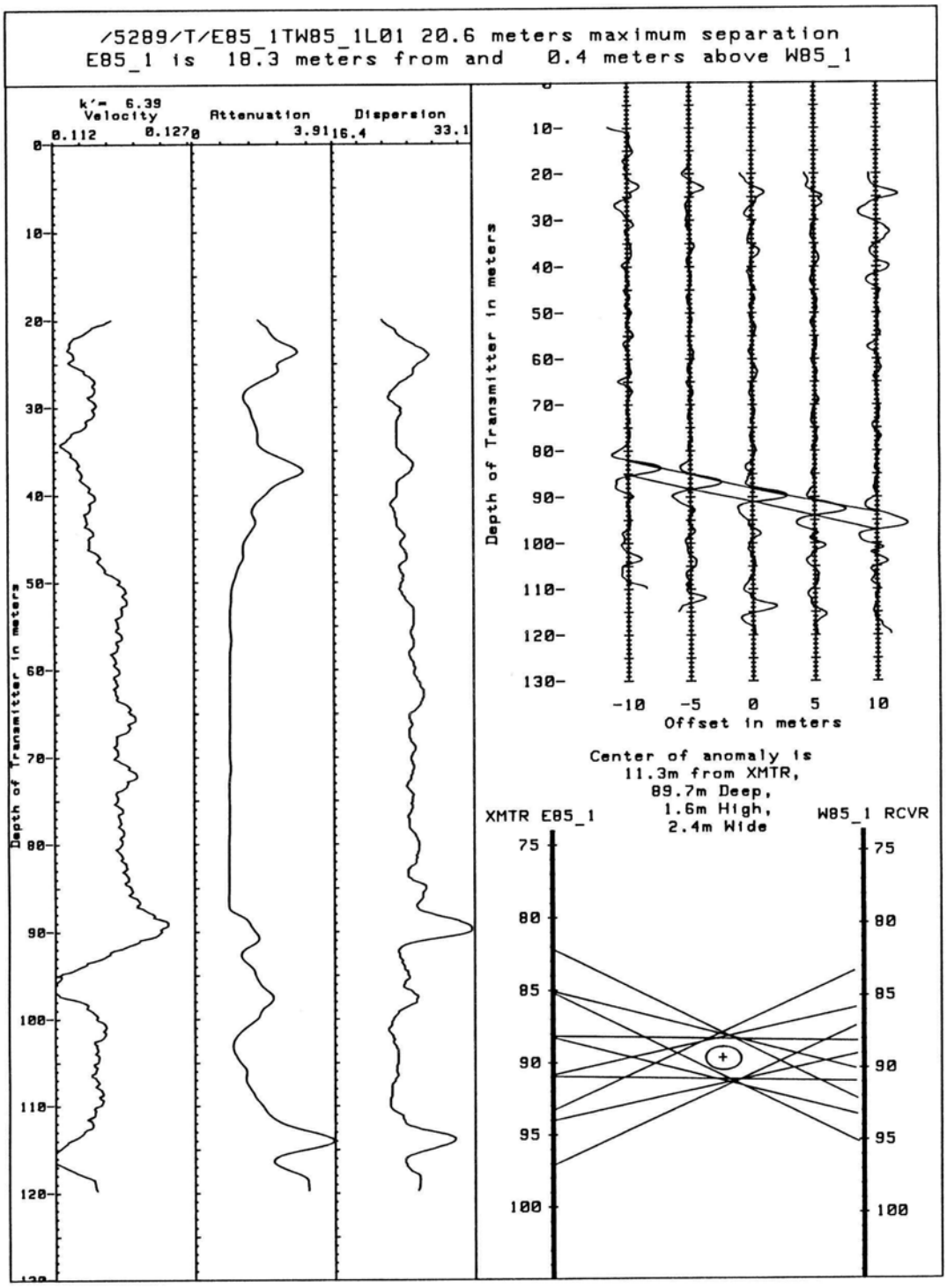

Figure 5 - The velocity, apparent attenuation and dispersion logs (left half of figure) and raypath inversion (right half) for the survey of a known tunnel. See text.

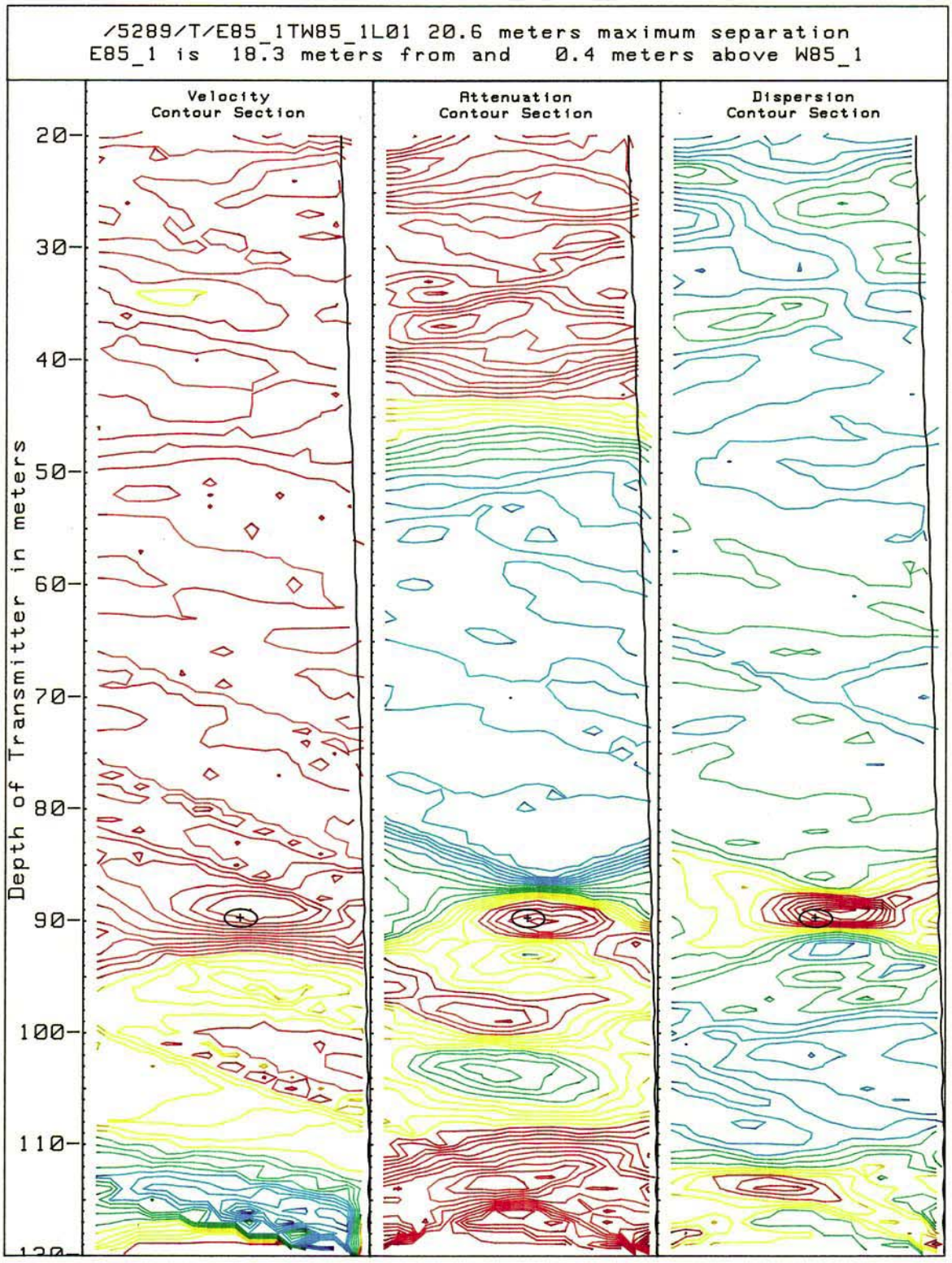

Figure 6 - The velocity, apparent attenuation and dispersion tomographic cross-sections for the same data as Figure 5. In all three, blue-green-yellow-red are low to high values.

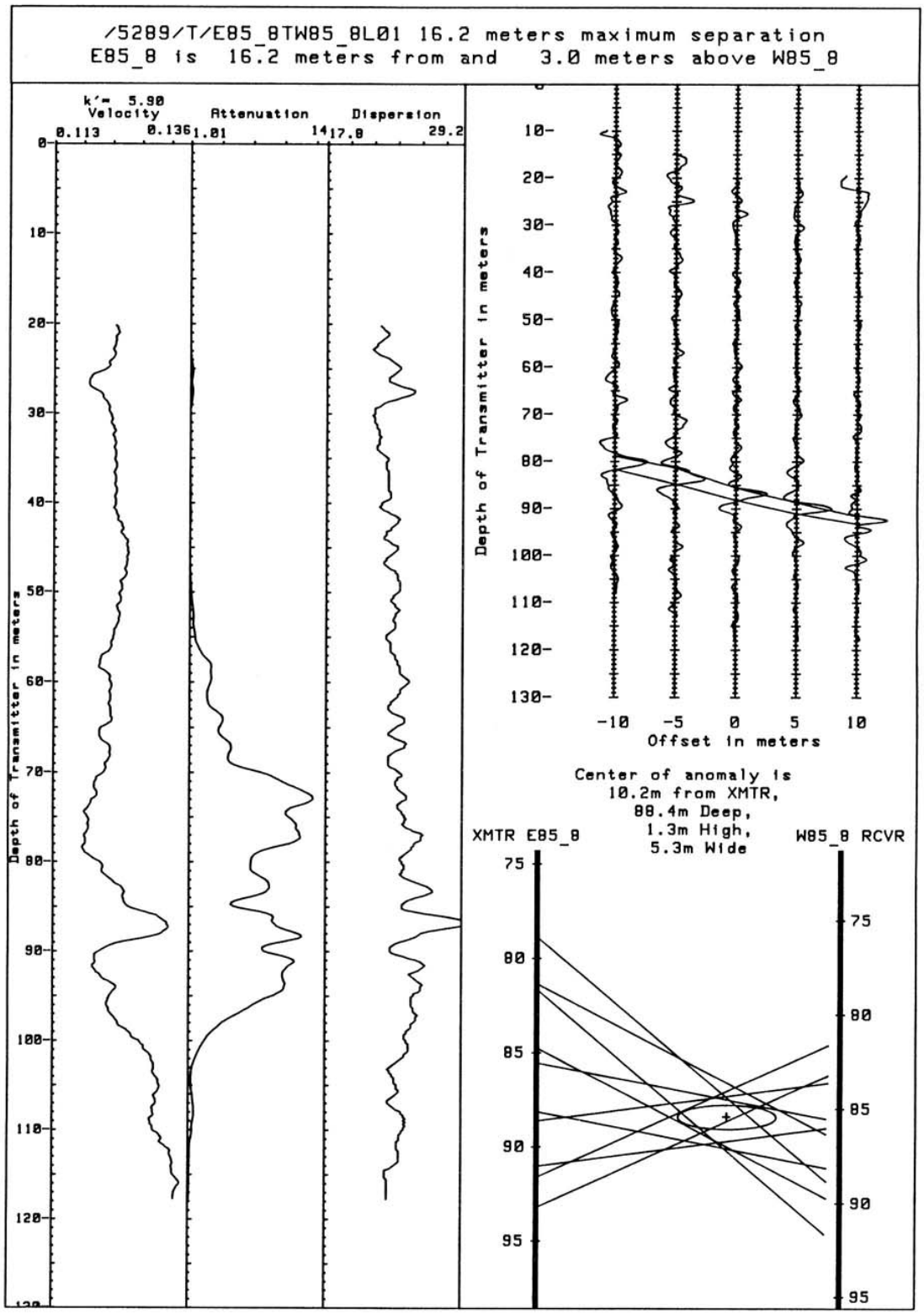

Figure 7 - The velocity, apparent attenuation and dispersion logs (left half of figure) and raypath inversion (right half) for the survey of a known tunnel. See text.

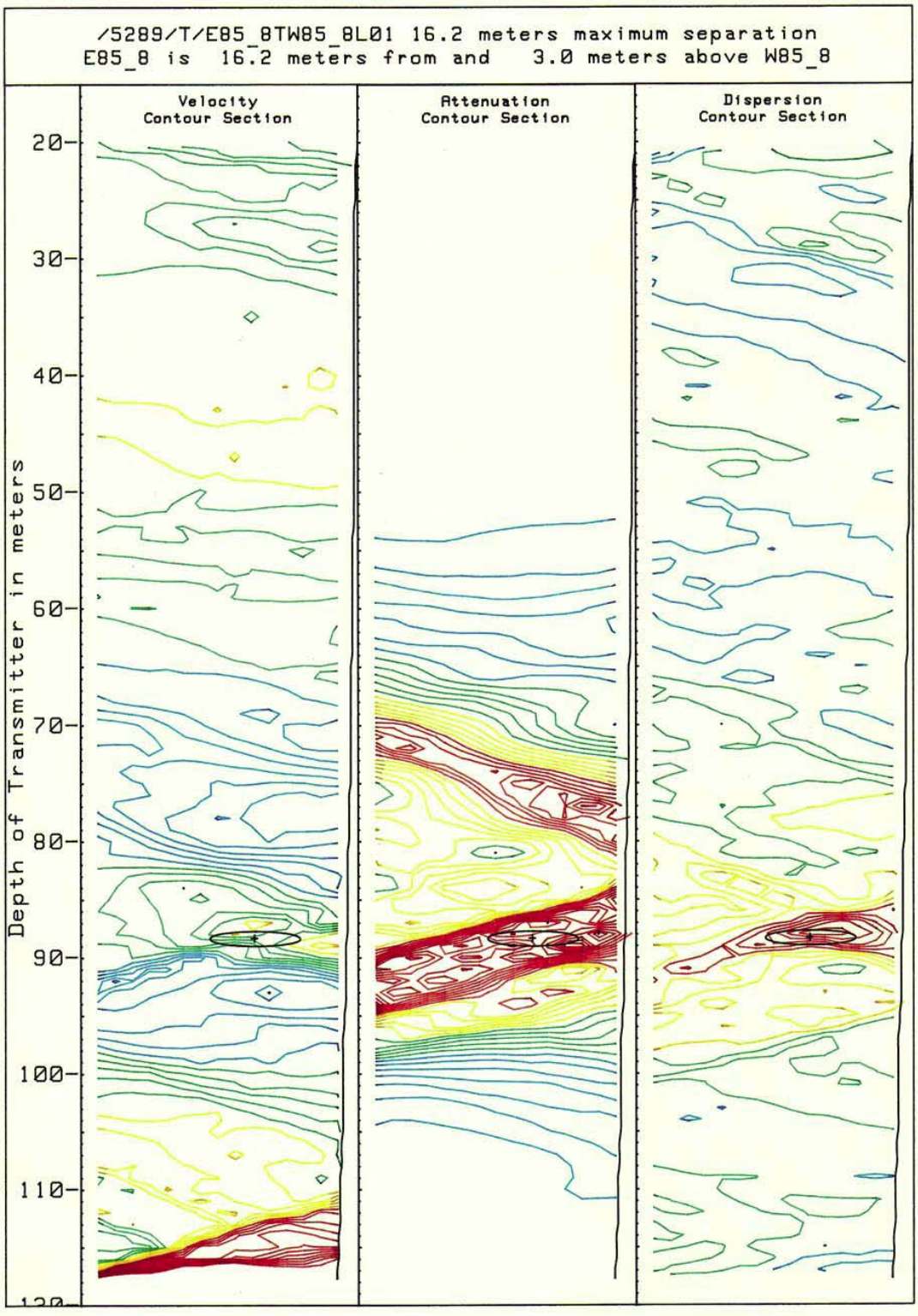

Figure 8 - The velocity, apparent attenuation and dispersion tomographic cross-sections for the same data as Figure 7. In all three, blue-green-yellow-red are low to high values.

Olhoeft, G. R., 1993, Velocity, attenuation, dispersion and diffraction hole-to-hole radar processing: in Proc. of the Fourth Tunnel Detectior Symp. on Subsurface Exploration Technology, Colorado School of Mines, Golden, CO, 26-29 April 1993, R. Miller, ed.: U.S.Army Belvoir Researc Development and Engineering Center, p. 309-322.

Velocity, Attenuation, Dispersion and Diffraction Hole-to-Hole Radar Processing

by

Gary R. Olhoeft
U.S. Geological Survey
P.O. Box 25046 DFC MS964
Denver, CO 80225-0046

Computer programs have been developed to automatically process hole-to-hole radar data without operator intervention. One version of the program takes the PEMSS (Pulsed Electromagnetic Search System; Owen, 1981) raw ground penetrating radar data, PEMSS II calibration data (if available), borehole deviation logs, and borehole 3D survey coordinates to produce:

1) apparent velocity, attenuation and dispersion logs versus depth for each offset,
2) self-consistency test error estimates,
3) raypath inversion to locate the principle anomaly,
4) multipath and diffraction analyses to size the anomaly (assuming a cylindrical air-filled void),
5) tomographs of apparent velocity, attenuation and dispersion in the plane between the boreholes to show surrounding geology,

and 6) three-dimensional perspective views of the tomographs to show geometry.

In order to accomplish this, first arrivals must be automatically picked. Several different first arrival pickers are used to handle noisy and distorted data, with the consensus (weighted with the location of the previous pick) chosen as the first arrival wavelet to process. Next, the datasets are subjected to a variety of self-consistency tests to determine the impact of errors on further tomographic processing or modeling. The largest errors occur from inadequate knowledge of the location of the logging tools in three dimensional space. Small corrections (meter-scale) can be inferred from the datasets themselves, larger errors require re-collection of the data. Then processing and modeling are performed, and lastly, several interpretive plots are generated. The raypath inversion accurately locates the depth and height of the tunnel (assuming straight ray paths), but exaggerates the width from the limited angular coverage during data acquisition. The diffraction and multipath modeling accurately determines the height of the tunnel (assuming an air-filled cylindrical void). The tomography confirms the character of the anomaly as an air-filled tunnel with velocity, attenuation and dispersion high compared to the surrounding rock and also provides geological context for the location of the tunnel between the borehole pair.

Presented to Fourth Tunnel Detection Symposium on Subsurface Exploration Technology, Colorado School of Mines, Golden, CO, April 26-29, 1993.

Velocity, Attenuation, Dispersion and Diffraction Hole-to-Hole Radar Processing

by Gary R. Olhoeft

Introduction

The acquisition of large amounts of hole-to-hole radar data on a production basis requires automatic processing and interpretation methods. The PEMS_GRO_10 program (discussed in this paper and in use since April, 1990) allows completely automatic and unattended processing of PEMSS I and PEMSS II (Pulsed Electromagnetic Search System)(Owen, 1981) data. PEMSS data processing (Kemerait and others, 1988; Olhoeft, 1988) and modeling (Greenfield, 1988; Moran, 1989) have been the subject of several papers in this and previous tunnel detection symposia.

The PEMS_GRO_10 program has built in safeguards to test the quality of data before processing. Inconsistent data can be processed, but with misleading or erroneous results. The program was designed to process a multiple sequence of data sets, flagging and labelling those with errors, and processing the good datasets to completion. Relatively unskilled personnel can keep data flowing into the system.

Data Acquisition

Hole-to-hole radar data are acquired by logging a pair of boreholes repeatedly. The transmitter is placed in one hole and the receiver in the other hole. Depths are recorded relative to the center of the transmitter tool. Both tools are simultaneously moved slowly and continuously during logging with a vertical depth offset between the transmitter and receiver. Several logging runs at different offsets are performed: typically -10, -5, 0, +5 and +10 meters (receiver relative to transmitter). A separate field crew acquires the hole survey location information and hole deviation logs.

Errors and Inconsistencies

In order to process hole-to-hole radar data (Olhoeft, 1988), the location of the holes must be known in three dimensional space (with surveys of the top of the holes at ground surface and borehole deviation surveys with depth). Inaccuracies in the knowledge of the positions of the holes and of the radar transmitter and receiver logging tools in the holes during data acquisition are the most significant errors in the entire data acquisition process. These errors propagate through data processing and modeling to produce artifacts in the final output that can lead to misleading or erroneous interpretation. Other sources of error include missing data, duplicate data (such as identical deviation logs for two different holes), clipped data, instrument error, excessive noise, and so forth. After the first arrivals are picked, a self-consistency test is performed on the entire data set to determine its overall quality before proceeding with tomography and modeling.

Data Processing and Modeling

The data are parameterized as described in Olhoeft (1988). A first arrival picker uses the consensus of a variety of methods to find the first arriving wavelet. The raypath distance between transmitter and receiver divided by the arrival time of the wavelet yields velocity. The reciprocal of the product of raypath distance times first arrival wavelet amplitude is apparent attenuation. Calibrated attenuation requires correction for the antenna patterns (which are unknown). The peak-to-peak broadening of the wavelet shape is used as an apparent dispersion (a measure of frequency dependence in velocity and attenuation). Calibrated dispersion requires wideband processing and correction for frequency dependent system characteristics (which are unknown).

To determine the quality and consistency of the entire dataset, the first arrival times are used with the given survey and deviation coordinates to perform a consistency test. The square of the ratio of the speed of light in vacuum to the velocity in the ground is the relative dielectric permittivity. For each offset between transmitter and receiver, the apparent relative permittivity is plotted versus the probe perturbation from its nominal position. The apparent relative permittivity is computed using first arrival time and raypath distance for the perturbed receiver tool position. A set of curves such as shown in Figure 1 for five offsets is generated. These curves are averages for the entire hole-pair dataset. If the dataset is consistent and there are no errors in instrument timing nor knowledge of the tool positions, the five curves should intersect at probe deviation equal to zero and the relative dielectric permittivity of the medium. In practice, some error occurs, so there is a spread in the intersections of the five curves. This spread is an indication of the quality of the overall dataset. In Figure 1, a box is drawn around the intersection showing +-0.5 units error in permittivity and +-0.5 meter error in position. The curve just skirting the lower edge of the box is the zero offset level run (transmitter and receiver run at same depth), not intersecting the remaining curves, and indicative of a timing error in that run. The entire dataset is marginally acceptable for further processing. In rock with large natural variations in electrical properties, it may be necessary to perform this test piecewise over uniform lithological sections or to use modal statistical analysis instead of the averages for the entire dataset.

For each offset between transmitter and receiver, a set of data is produced (similar to wireline logs) consisting of tool separation, hole-to-hole velocity, apparent attenuation and apparent dispersion, each versus depth. The left half of Figure 2 illustrates the zero offset set of such data for one hole pair. A summary (as the product of velocity times dispersion versus depth) of the multiple offsets is shown in the upper right part of Figure 2. The lines connecting the most significant anomaly in each offset are used in the lower right part of Figure 2 to locate the anomaly by raypath inversion between the two holes. The outer ellipse represents the locus of the possible centers for the anomaly, while the inner ellipse represents the probable size of the anomaly.

The offset data are then run through a filtered back projection algorithm (Olhoeft, 1988, and references therein) to produce velocity, apparent attenuation and apparent dispersion tomographs as shown in Figure 3. The plus surrounded by two ellipses is the raypath inversion from Figure 2. Note the borehole deviation on the right edge of each panel. Everything is plotted relative to the transmitter hole (on the left edge of each panel). An air filled mined tunnel appears as a velocity high (red contours) as the speed of light is higher in air than in rock. It appears as an attenuation high from scattering of energy at the tunnel walls (and possibly from enhanced electrical conductivity in the crack halo around the tunnel, Pusch, 1989). It appears as a dispersion high from the distortion of the wavelet caused by

frequency dependent scattering (the tunnel is about the size of the radar wavelength in the rock; Olhoeft, 1988) or from constructive and destructive multipath interference.

The approximate location of the center of the anomaly from raypath inversion is then used to find the maximum anomaly in the zero offset level run data. In Figure 4, on the left half of the plot are shown a portion of the level run data centered on the maximum anomaly. Assuming a circular cross-section, air-filled void, the right half of Figure 4 is an attempt to model the electromagnetic waves around, through and scattered from the tunnel. The yellow color represents waves through the rock with no apparent effect from the tunnel. The red color shows where the waves go through the tunnel and recombine with waves that leak around the tunnel, producing multipath constructive and destructive interference. The green color traces out the complex parabola from diffracted waves, scattered off the tunnel walls. Such full waveform diffraction modeling improves the resolution of the size and shape of the void by up to an order of magnitude. If such diffractions are evident in all of the offset data, diffraction tomography (Witten and King, 1988) may be performed. However, diffraction tomography is typically possible in only a few percent of the data. Either there are too many diffractions and they can't be clearly sorted out, or there are few diffractions to be exploited. Figure 4 shows an example of negligible diffractions. The tunnel is still visible in the data, but the resolution-enhancing improvement possible with diffraction tomography cannot be exploited in this data set. Diffraction modeling only provides a limit to the size of the tunnel. Figures 5 through 8 illustrate a clear example of hole-to-hole radar data for a similar sized tunnel in similar geological material, but causing strong diffractions. The factors determining the presence or absence of strong diffractions have not been investigated. However, they are probably related to changes in the rough walled faceting of the tunnels as the diffractions have been observed to come and go along the length of the same tunnel in the same material, and with differing transmitter-receiver offsets (or radar viewing angles of the tunnel).

Discussion

All of the figures in this paper were produced automatically and without operator interaction. Figures 1 to 4 are an uncalibrated PEMMS I set from one tunnel site, and Figures 5 to 8 are a calibrated PEMSS II set from a second tunnel site. Calibrated refers to the accuracy of the time base and knowledge of the location of time zero. Greater drift in the PEMSS I time base produces higher inconsistency in PEMSS I data than in PEMSS II data. Also, much of the archival PEMSS I data was not calibrated to test the time base and locate time zero (by measuring the travel time through air with the transmitter and receiver at known separation). The surveying, deviation and PEMSS data were placed into a database accessible to the PEMS_GRO_10 program, and the program executed. All of the data were automatically processed and plotted as shown. Accompanying datasets which contained inconsistencies or missing components were flagged for operator attention. The raypath inversion accurately locates the depth and height of the tunnel (assuming straight ray paths), but exaggerates the width from the limited angular coverage during data acquisition. The diffraction and multipath modeling accurately determines the height of the tunnel (assuming an air-filled cylindrical void). The tomography confirms the character of the anomaly as an air-filled tunnel with velocity, attenuation and dispersion high compared to the surrounding rock, and they also provide geological context for the location of the tunnel between the borehole pair (in other words, the homogeneity of the rock surrounding the tunnel).

Finally, three-dimensional perspective views of the tomograms are presented to show the true spatial relationships between the tunnel and surrounding geology, with the ability to zoom in and out, and to tilt and rotate the 3D views on the graphics display of a workstation (see example in Wright and others, 1993).

Acknowledgement

This work was funded by the U. S. Army Belvoir Research, Development and Engineering Center, Ft. Belvoir, Virginia.

References

Greenfield, R. J., 1988, Modeling of electromagnetic propagation between boreholes: in Third Technical Symposium on Tunnel Detection Proceedings, Jan. 12-15, 1988, Colorado School of Mines, Golden, CO, p. 156-172.

Kemerait, R. C., Griffin, J. N., Meade, J. L., Kraft, G. D. and Pound, G. W., 1988, Signal processing applied to tunnel detection by borehole radar: in Third Technical Symposium on Tunnel Detection Proceedings, Jan. 12-15, 1988, Colorado School of Mines, Golden, CO, p. 593-615.

Moran, M., 1989, Time domain analysis of electromagnetic scattering for a three dimensional tunnel in the presence of a vertically oriented electric dipole: MSc thesis, Dept. of Geosciences, Pennsylvania State Univ., State College, PA, var. pag.

Olhoeft, G. R., 1988, Interpretation of hole-to-hole radar measurements: in Third Technical Symposium on Tunnel Detection Proceedings, Jan. 12-15, 1988, Colorado School of Mines, Golden, CO, p. 616-629.

Owen, T. R., 1981, Cavity detection using VHF hole-to-hole electromagnetic techniques: Second Tunnel Detection Symposium, Colorado School of Mines, Golden, CO, July 21-23, 1981, U. S. Army MERADCOM, Ft. Belvoir, VA, p. 126-141.

Pusch, R., 1989, Influence of various excavation techniques on the structure and physical properties of "near-field" rock around large boreholes: Svensk Karnbranslehantering AB (Swedish Nuclear Fuel and Waste Management Co.) Technical Report 89-32, Stockholm, Sweden, 57p.

Witten, A. J. and King, W. C., 1988, Geophysical diffraction tomography for imaging isolated subsurface inclusions: in Third Technical Symposium on Tunnel Detection Proceedings, Jan. 12-15, 1988, Colorado School of Mines, Golden, CO, p. 227-241.

Wright, D. L., Olhoeft, G. R., Grover, T. P., and Bradley, J. A., 1993, High-speed digital radar systems and applications to subsurface exploration: Fourth Tunnel Detection Symposium on Subsurface Exploration Technology, Colorado School of Mines, Golden, CO, April 26-29, 1993, this volume.

Figure Captions

Figure 1

Self-consistency test of the dataset for Figures 1 to 4. The apparent relative dielectric permittivity is plotted versus perturbed receiver probe position for each of the five transmitter-receiver depth offsets (expressed as probe deviation from its nominal position). All the curves should intersect at a point above deviation zero and at the true relative permittivity of the medium in the absence of errors. The box is +-0.5 dielectric units by +-0.5 meters in size, outlining the acceptable locus of spread in the intersection of the curves. The relative dielectric permittivity is 6.06 +- 0.27.

Figure 2

The left half of this figure shows the velocity, apparent attenuation and apparent dispersion logs for the level run at this site. The upper right quarter of the figures shows the velocity-dispersion product for the five offsets. The lower right portion of the plot shows the ray path inversion of the largest anomaly in the upper right set of offsets. The outer ellipse is the possible location of the center of the anomaly and the inner ellipse is its probable size.

Figure 3

The velocity, apparent attenuation and apparent dispersion tomographs for the site in Figures 1, 2 and 4. In each case, the spectrum blue through red is low to high, and the plus surrounded by ellipses is the raypath inversion from the previous figure.

Figure 4

The left half is the original data and the right half is the diffraction and multipath model. The yellow coded curves represent the radiowaves travelling through the rock with no influence from the tunnel. The red coded curves represent the waves travelling through the tunnel and combining constructively and destructively with the waves leaking around the tunnel. The green coded curves are the waves diffracting off of the tunnel.

Figures 5 to 8 are the same as Figures 1 to 4, though for a different tunnel at another site exhibiting strong diffraction events.

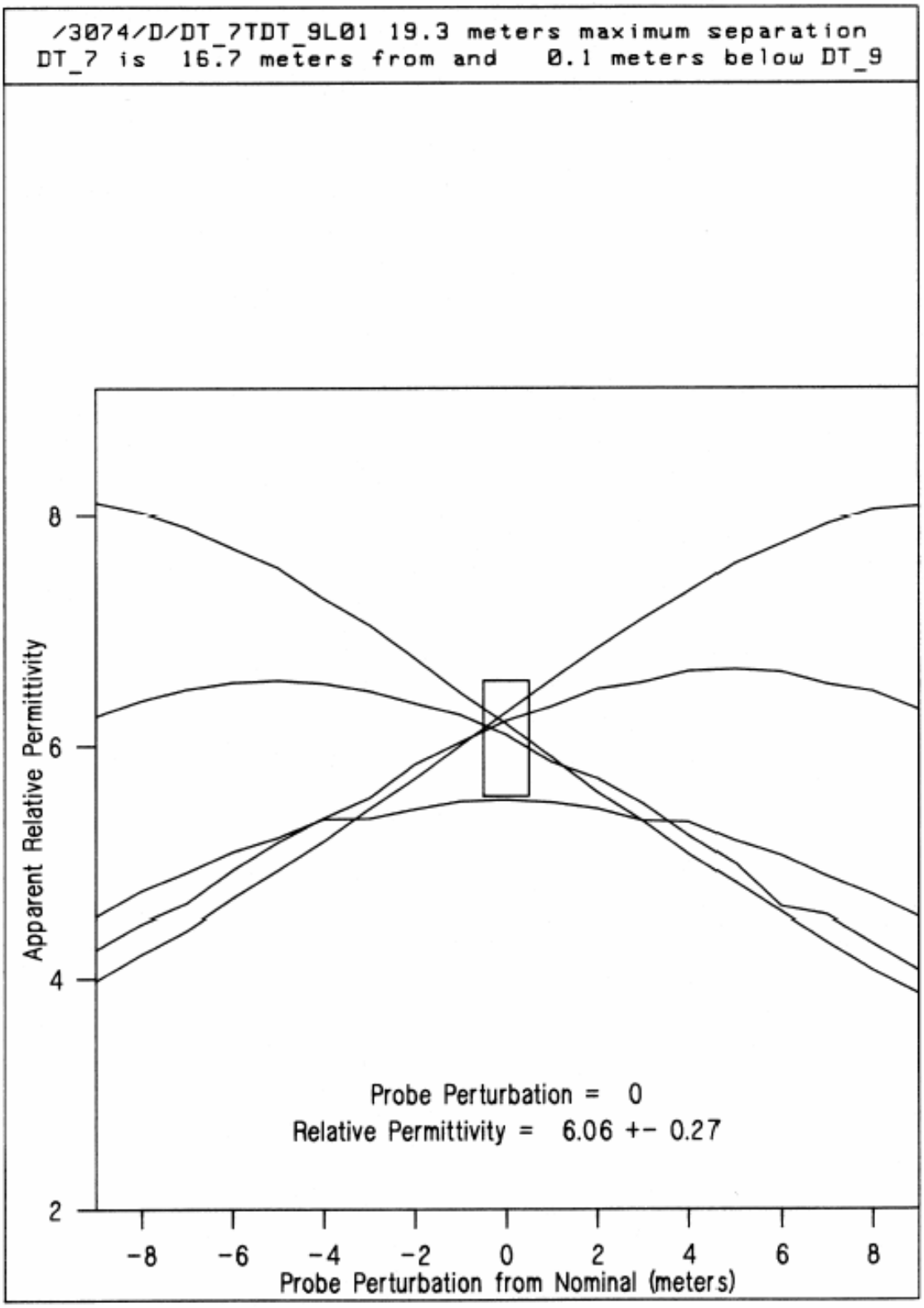
/3074/D/DT_7TDT_9L01 19.3 meters maximum separation
DT_7 is 16.7 meters from and 0.1 meters below DT_9
Apparent Relative Permittivity
8
6
4
2
Probe Perturbation = 0
Relative Permittivity = 6.06 +- 0.27
-8
-6
-4
-2
0
2
4
6
8
Probe Perturbation from Nominal (meters)

Figure 1

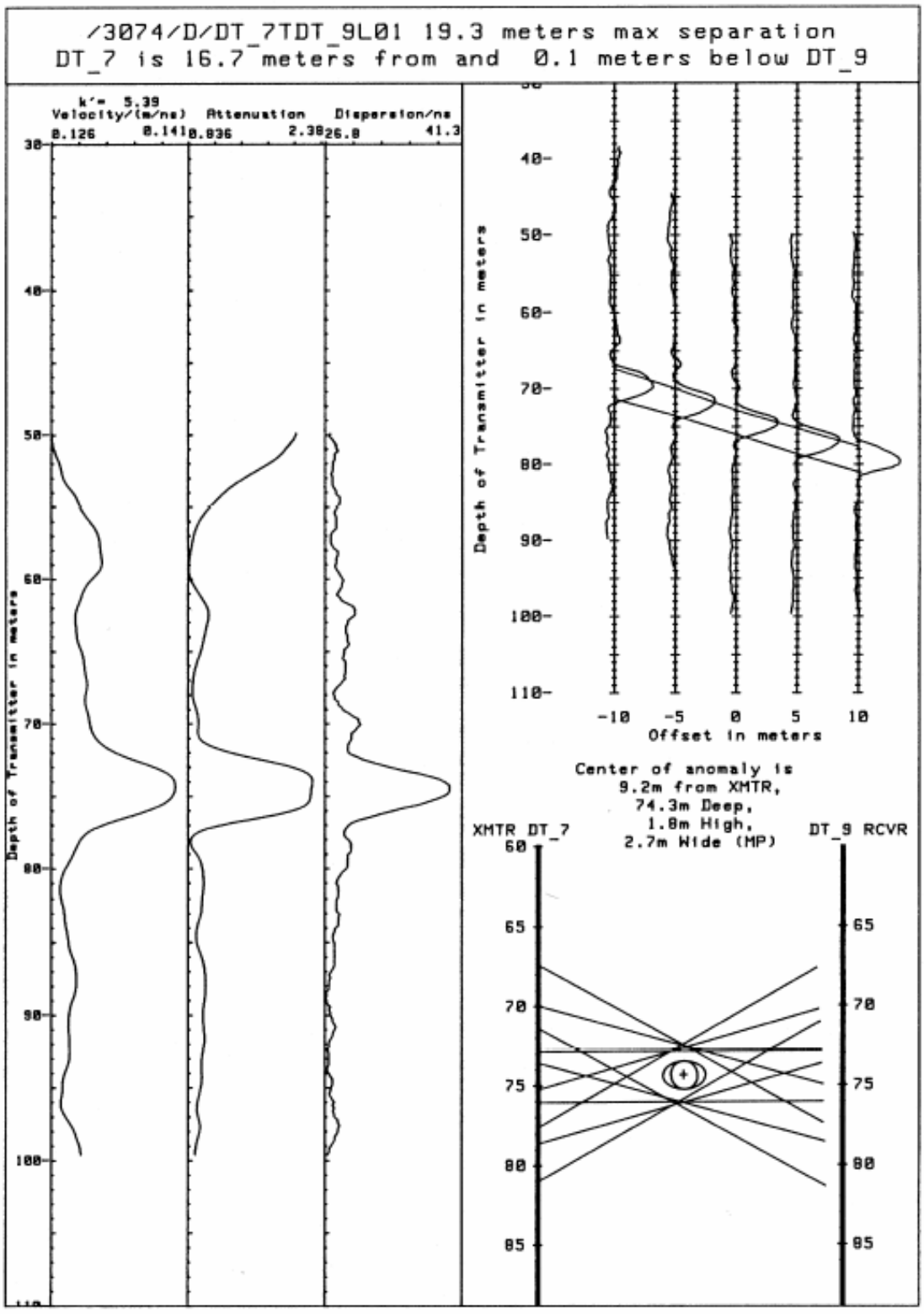
/3074/D/DT_7TDT_9L01 19.3 meters max separation
DT_7 is 16.7 meters from and 0.1 meters below DT_9
k'= 5.39
Velocity/(m/ns)
Attenuation
Dispersion/ns
8.126
8.141
8.836
2.38
26.8
41.3
Depth of Transmitter in meters
Offset in meters
-10
-5
0
5
10
Center of anomaly is
9.2m from XMTR,
74.3m Deep,
1.8m High,
2.7m Wide (MP)
XMTR DT_7
DT_9 RCVR

Figure 2

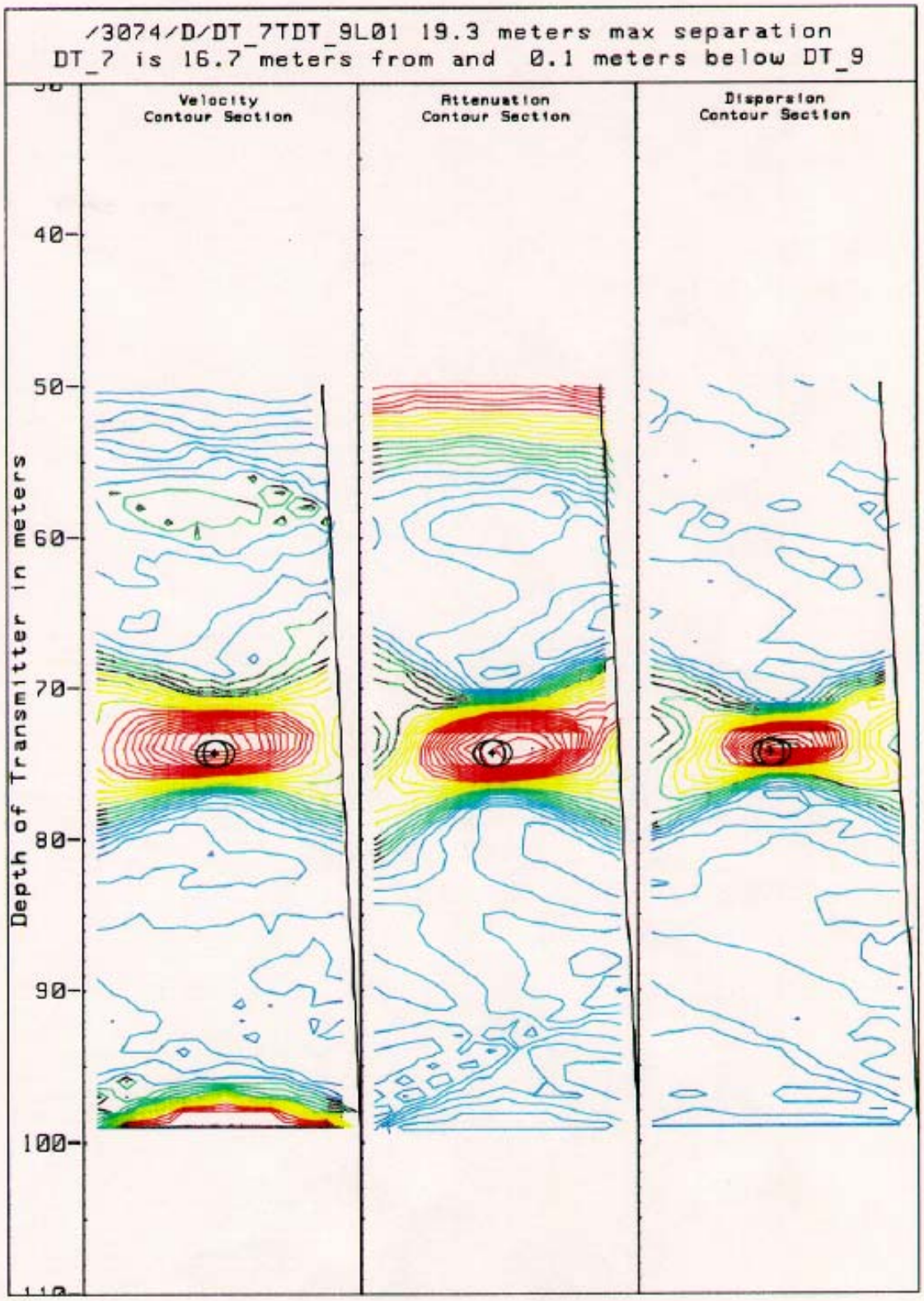
/3074/D/DT_7TDT_9L01 19.3 meters max separation
DT_7 is 16.7 meters from and 0.1 meters below DT_9
Velocity
Contour Section
Attenuation
Contour Section
Dispersion
Contour Section
Depth of Transmitter in meters
40
50
60
70
80
90
100

Figure 3

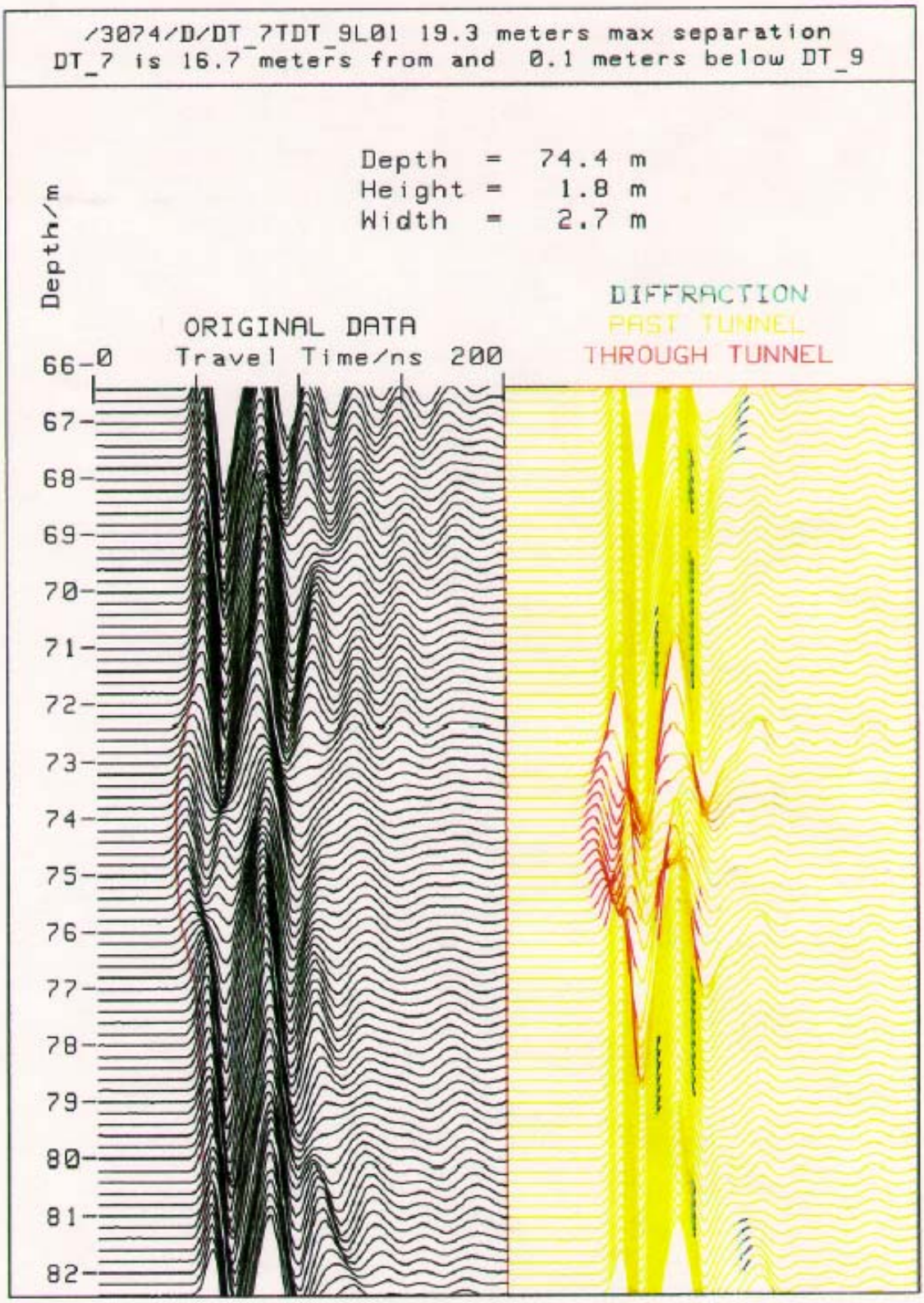
/3074/D/DT_7TDT_9L01 19.3 meters max separation
DT_7 is 16.7 meters from and 0.1 meters below DT_9
Depth = 74.4 m
Height = 1.8 m
Width = 2.7 m
Depth/m
ORIGINAL DATA
Travel Time/ns
0
200
DIFFRACTION
PAST TUNNEL
THROUGH TUNNEL
66
67
68
69
70
71
72
73
74
75
76
77
78
79
80
81
82

Figure 4

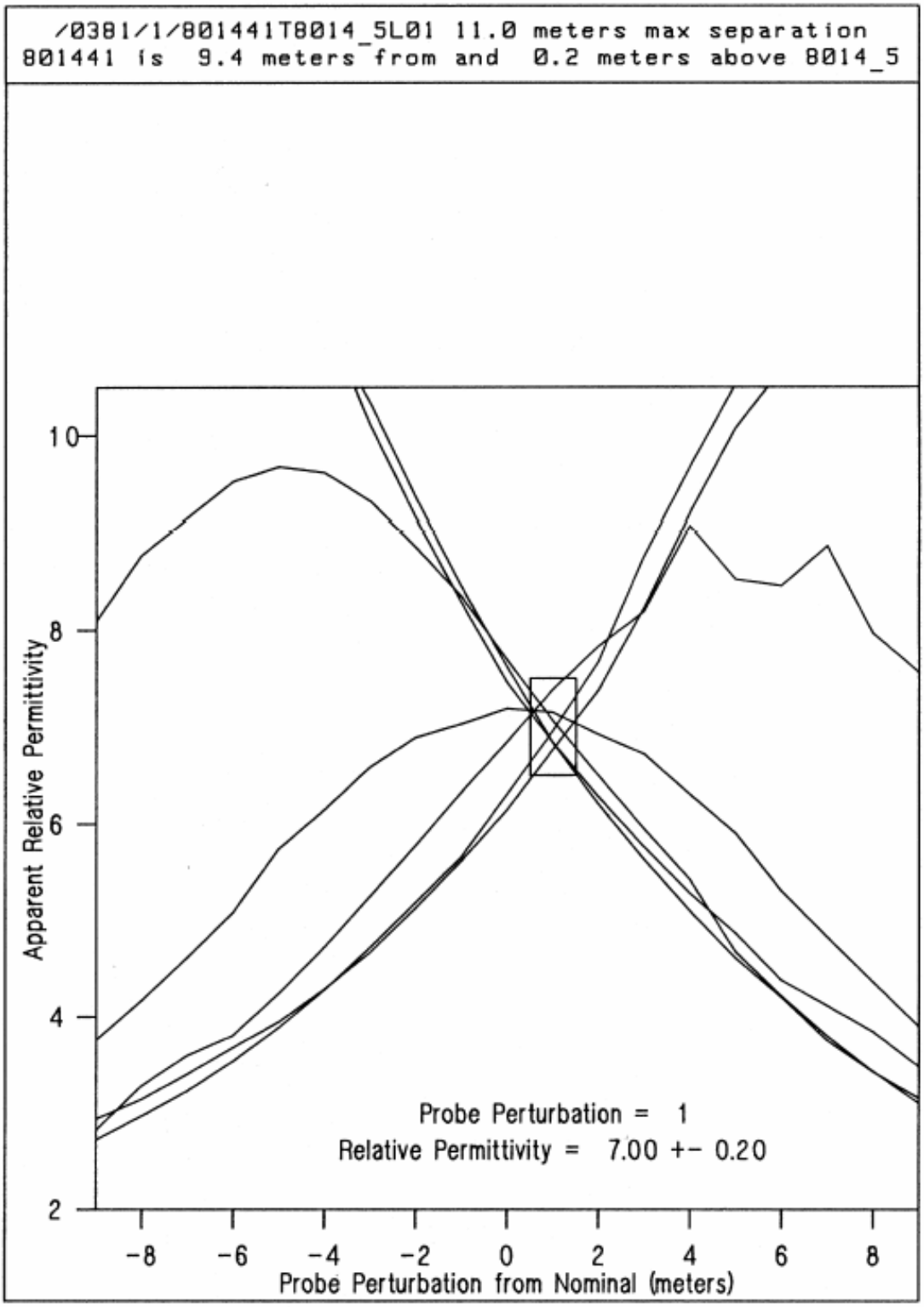
/0381/1/801441T8014_5L01 11.0 meters max separation
801441 is 9.4 meters from and 0.2 meters above 8014_5
Apparent Relative Permittivity
10
8
6
4
2
Probe Perturbation = 1
Relative Permittivity = 7.00 +- 0.20
-8
-6
-4
-2
0
2
4
6
8
Probe Perturbation from Nominal (meters)

Figure 5

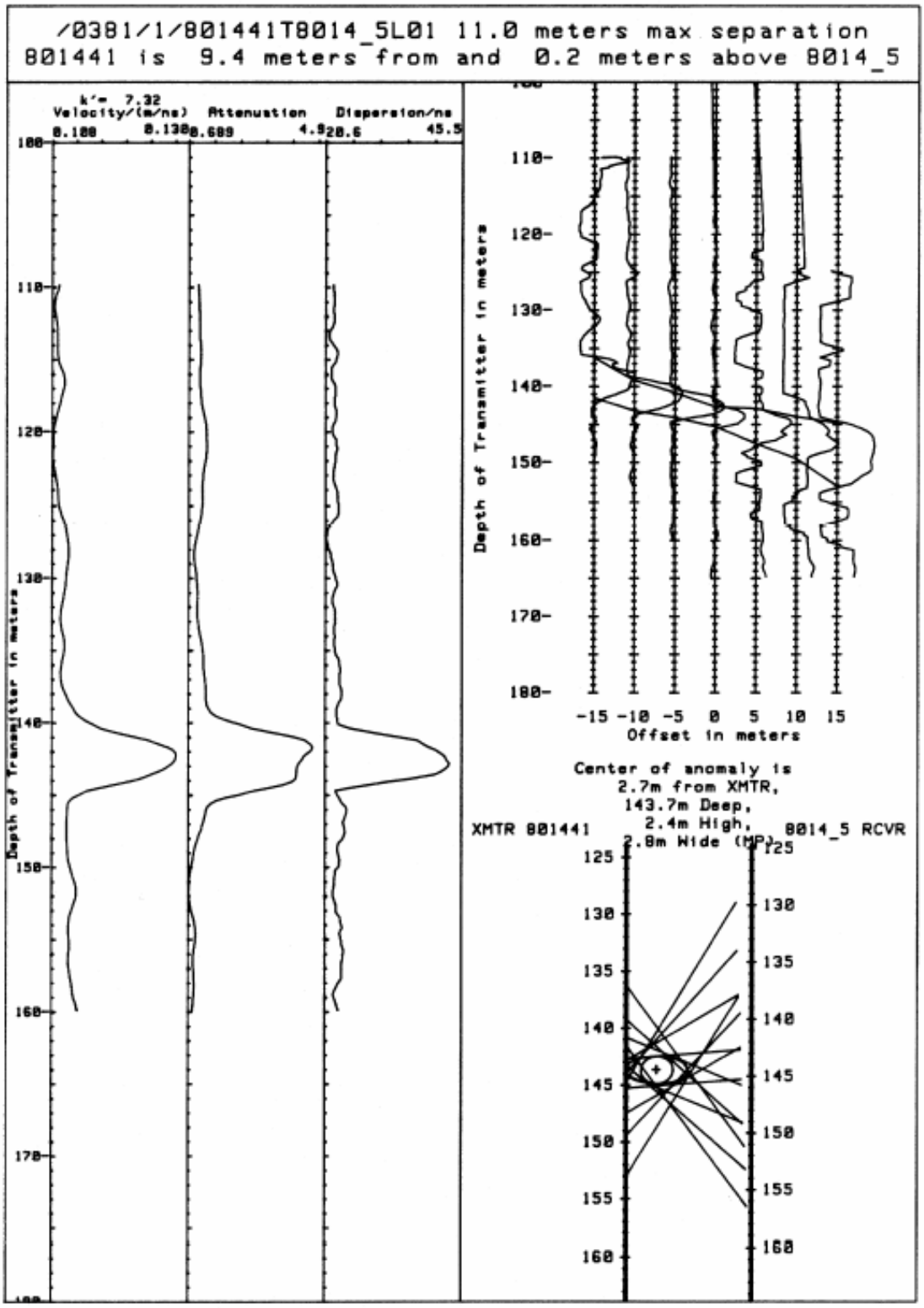
/0381/1/801441T8014_5L01 11.0 meters max separation
801441 is 9.4 meters from and 0.2 meters above 8014_5
k'= 7.32
Velocity/(m/ns)
Attenuation
Dispersion/ns
0.188
0.138
8.689
4.9
28.6
45.5
Depth of Transmitter in meters
Offset in meters
-15 -10 -5 0 5 10 15
Center of anomaly is
2.7m from XMTR,
143.7m Deep,
2.4m High,
2.8m Wide (MP)
XMTR 801441
8014_5 RCVR

Figure 6

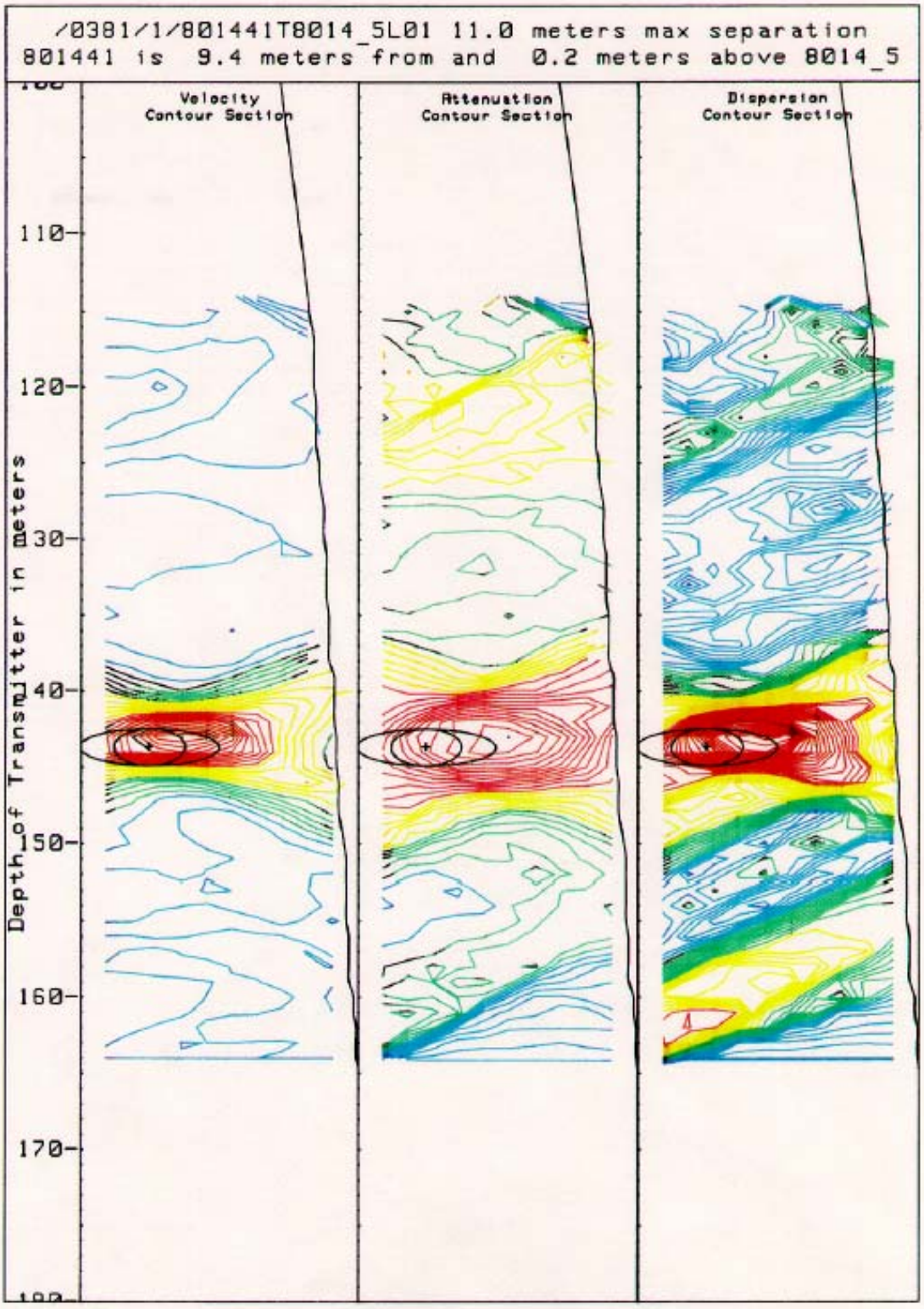
/0381/1/801441T8014_5L01 11.0 meters max separation
801441 is 9.4 meters from and 0.2 meters above 8014_5
Velocity Contour Section
Attenuation Contour Section
Dispersion Contour Section
Depth of Transmitter in Meters
110
120
130
140
150
160
170

Figure 7

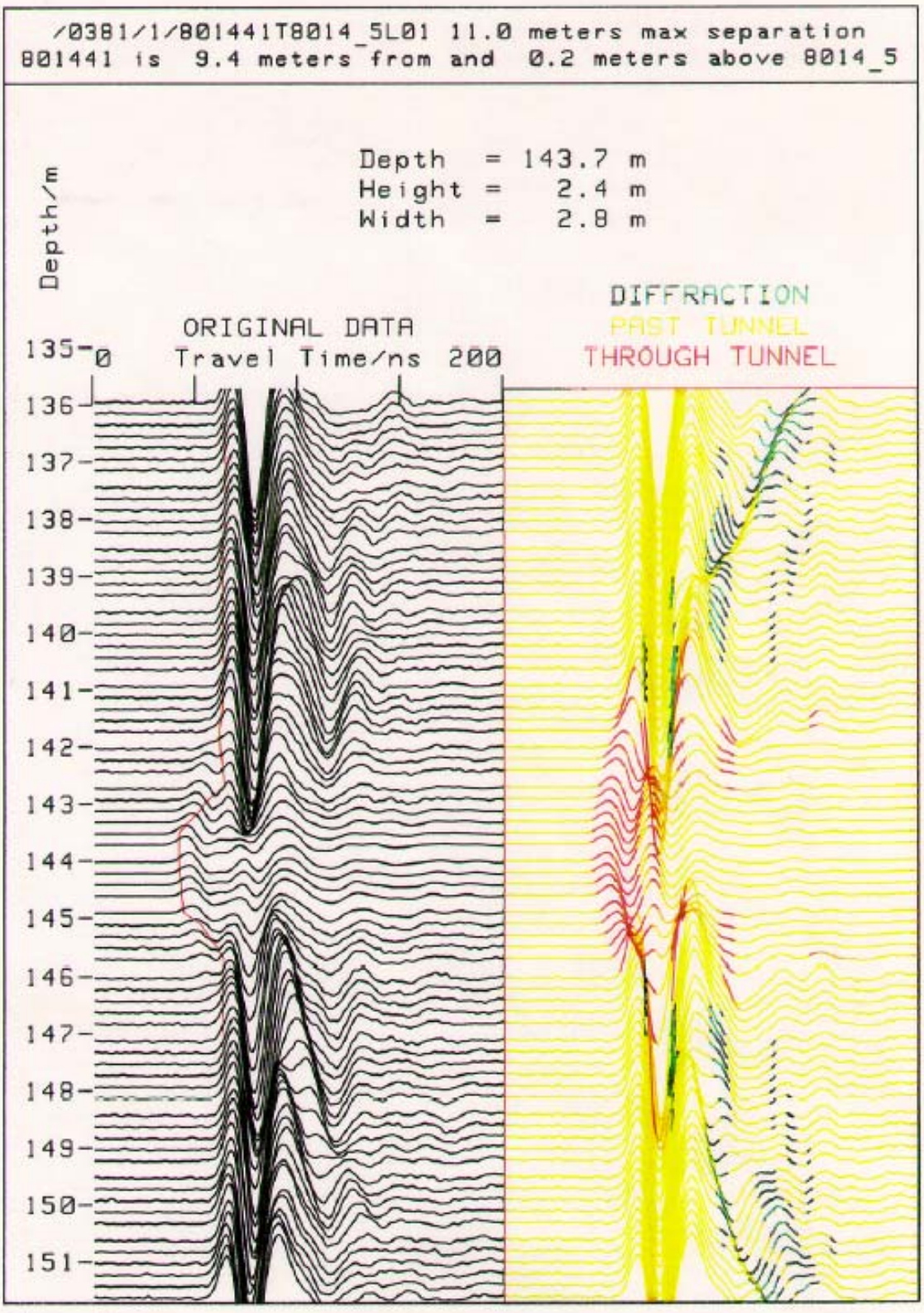
/0381/1/801441T8014_5L01 11.0 meters max separation
801441 is 9.4 meters from and 0.2 meters above 8014_5
Depth = 143.7 m
Height = 2.4 m
Width = 2.8 m
Depth/m
ORIGINAL DATA
Travel Time/ns
0
200
DIFFRACTION
PAST TUNNEL
THROUGH TUNNEL
135
136
137
138
139
140
141
142
143
144
145
146
147
148
149
150
151

Figure 8